

History and physical principles of MRI

Michael E. Hayden, Pierre-Jean Nacher

▶ **To cite this version:**

Michael E. Hayden, Pierre-Jean Nacher. History and physical principles of MRI. Luca SABA. Magnetic Resonance Imaging Handbook, 1, CRC press, 2016, 978-1482216288. hal-01191404

HAL Id: hal-01191404
https://hal.science/hal-01191404

Submitted on 2 Sep 2015

HAL is a multi-disciplinary open access archive for the deposit and dissemination of scientific research documents, whether they are published or not. The documents may come from teaching and research institutions in France or abroad, or from public or private research centers.

L'archive ouverte pluridisciplinaire **HAL**, est destinée au dépôt et à la diffusion de documents scientifiques de niveau recherche, publiés ou non, émanant des établissements d'enseignement et de recherche français ou étrangers, des laboratoires publics ou privés.



Distributed under a Creative Commons Attribution - NonCommercial 4.0 International License

History and physical principles of MRI

Michael E. Hayden[1] and Pierre-Jean Nacher[2]

[1] *Physics Department, Simon Fraser University, 8888 University Drive, Burnaby BC, Canada*
[2] *Laboratoire Kastler Brossel, ENS-PSL Research University, CNRS, UPMC-Sorbonne Universités, Collège de France; 24 Rue Lhomond, F75005 Paris, France*

Magnetic Resonance Imaging was broadly introduced to the scientific community in 1973, when Paul C. Lauterbur published images representing the Nuclear Magnetic Resonance response of hydrogen nuclei in a pair of water-filled glass capillaries [1]. One-dimensional (1-D) projections of this response were first obtained through a procedure that involved applying static magnetic field gradients to the sample, mapping NMR frequency onto source position. A series of 1-D projections, acquired along different gradient directions, were then combined to reconstruct a two-dimensional image, as illustrated in Fig. 1.

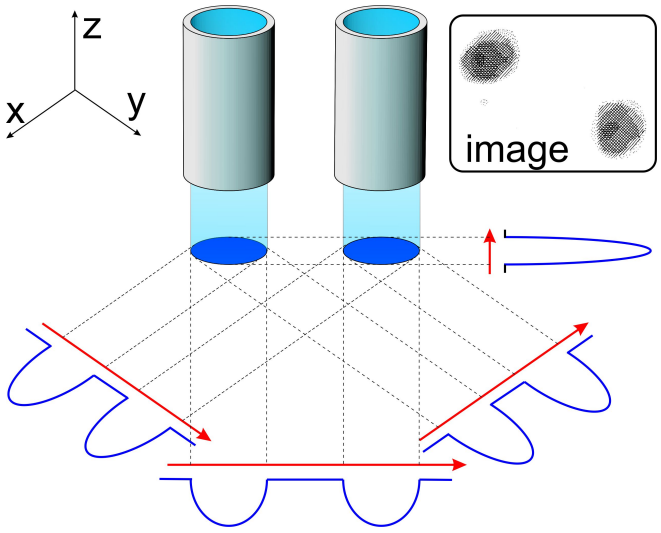


Figure 1: Principle underlying the first MR imaging experiment performed by P.C. Lauterbur [1]. Two objects (water-filled capillaries) aligned with the z-axis are shown, along with their projection onto the x-y plane. Magnetic field gradients applied along various directions cause the NMR response to spread out in frequency, producing one-dimensional projections reflecting the distribution of water (blue curves). Multiple projections, acquired along different gradient directions (indicated by red arrows), are then combined to reconstruct a two dimensional image. Inset: Lauterbur's NMR image of two 1 mm inner-diameter water-filled capillaries [1].

A new word for a new way of seeing

Lauterbur coined the term *zeugmatogram* to describe his NMR images. This word is derived from the Greek $\zeta\epsilon\upsilon\gamma\mu\alpha$ ("zeugma") meaning "that which is used for joining," in reference to the manner in which static magnetic field gradients were employed to localize the sample response to oscillating magnetic fields. Similar 1-D NMR imaging methods had already been demonstrated as early as 1952 [2] and were employed in the 1956 discovery of phase separation in liquid ^{3}He-^{4}He mixtures at low temperatures [3]. But, it was Lauterbur who extended the method to two dimensions and recognized its potential for soft tissue imaging. Perhaps the most well known 1-D NMR images predating Lauterbur's 1973 paper were published just one year earlier, in connection with a Cornell University study of another low temperature phase transition, this time in pure liquid ^{3}He [4]. Three of the four authors of that report were awarded the 1996 Nobel Prize in Physics for the discovery of superfluidity in ^{3}He.

The term *Zeugmatography* remains obscure, but *MRI* – the field that emerged – is anything but.

Lauterbur's simple but insightful demonstration launched a flurry of scientific, industrial, and clinical activity that has since profoundly influenced the practice and delivery of medicine in industrialized countries. Sophisticated extensions of his work are now fueling revolutions in neuroscience and our understanding of cognition.

This chapter starts by tracing the history of MRI from its roots in the field of NMR through to the present. It is a story that is much richer and nuanced than can be adequately described in a few pages; our narrative certainly ignores many critical contributions to the field. The basic physical principles of NMR are then introduced; these form the basis for understanding the "NMR response" referred to above. Again, the treatment presented here is necessarily brief. The interested reader is encouraged to consult some of the excellent and extensive monographs

that have been written on this topic [5, 6, 7, 8, 9, 10]. Finally the basic principles underlying Magnetic Resonance (MR) image generation itself are introduced; many of these topics are covered in greater detail in subsequent chapters, but again the interested reader will find valuable additional information about the underlying physics in more specialized references [11, 12, 13, 14, 15].

1 History

The foundations of Nuclear Magnetic Resonance – and hence Magnetic Resonance Imaging – were laid during the 1940s, in experiments designed to directly detect the precession of nuclear magnetic moments in a magnetic field [16, 17, 18]. Those experiments, which involved hydrogen atoms in liquids and solids, built on work carried out during the 1930s at Columbia University. There, a team led by Isidore I. Rabi showed that an oscillating magnetic field could be used to induce transitions between nuclear spin states of lithium and chlorine atoms in a molecular beam [19]. Rabi's pioneering experiments in turn employed spin-state selection and detection techniques similar to those developed in Frankfurt during the 1920s by Otto Stern and Walther Gerlach, in connection with their seminal discovery of spin quantization using a beam of silver atoms [20].

The extension of Rabi's 1938 observation of Nuclear Magnetic Resonance in a beam of independent molecules to solid and liquid samples was successfully, independently, and essentially simultaneously accomplished in 1945 by Edward M. Purcell and by Felix Bloch. A key feature of these experiments was the fact that both employed direct electromagnetic detection techniques to resolve the resonances. At the Massachusetts Institute of Technology (MIT) Radiation Laboratory, Purcell, Torrey, and Pound, worked with 1 litre of solid paraffin in a cavity tuned to resonate at 30 MHz. They observed a 0.4% change in radiofrequency (RF) signal amplitude across the cavity as the static magnetic field was swept through "an extremely sharp resonance"; this reduction in quality factor was attributed to energy dissipation associated with nuclear spin relaxation of H atoms [16]. Meanwhile at Stanford University, Bloch, Hansen, and Packard, performed similar experiments on a 1.5 cm^3 sample of water at 7.7 MHz. They used two orthogonal RF coils; the receive coil detected RF power when the nuclei of the water protons (H atoms) were resonantly excited by the transmit coil [18]. Although Rabi's work was crucial as the initial demonstration of NMR (he was awarded the Physics Nobel prize in 1944 "for his resonance method for recording the magnetic properties of atomic nuclei"), the conceptual and technical leap achieved by Bloch and Purcell really set the stage for the development of modern NMR and MRI.

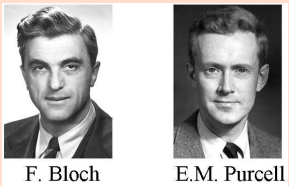
Early attempts and first successes

The first reported attempt to observe nuclear spin transitions in solids was published in 1936 by Cornelis J. Gorter [21], who was based in Leiden. That experiment failed, as did a later attempt described in a 1942 paper [22]. Gorter's second paper contains the first published reference to *nuclear magnetic resonance*, a term that he attributed to Rabi. Meanwhile in Kazan, Yevgeny Zavoisky also failed to reliably detect NMR transitions in solids and liquids, but went on to discover electron spin resonance (ESR) in 1944.



Reprinted with permission from (l-r): The Nobel Foundation; Eddy de Jongh; World Scientific.

The first truly successful NMR experiments on solids and liquids were reported in early 1946 [16, 17], by two independent teams. One of these teams was led by Felix Bloch at Stanford University. Bloch obtained a PhD from the University of Leipzig in 1928. He left Germany in 1933 and moved to Stanford University, where he spent most of his career. During the latter part of the second world war he spent time at the Harvard Radio Research Laboratory, where he worked on counter-radar measures and became acquainted with modern developments in electronics. The other team was led by Edward M. Purcell at MIT. Purcell obtained a PhD from Harvard in 1938. He spent the war years at the MIT Radiation Laboratory, where he was influenced by Rabi and contributed to the development of radar and various microwave techniques. He returned to Harvard in 1945, and spent the rest of his career there. Bloch and Purcell were awarded the 1952 Physics Nobel prize "for their development of new methods for nuclear magnetic precision measurements and discoveries in connection therewith."



Reprinted with permission from The Nobel Foundation.

A final critical component of the modern NMR toolbox was contributed independently by Henry C. Torrey [23]

and Erwin L. Hahn [24], who demonstrated the feasibility of pulsed NMR (an idea originally suggested by Bloch [25]) and observed free Larmor precession. Hahn further used pulsed NMR to generate and observe spin echoes [26].

The next 20 years saw the development of NMR as a powerful investigative tool in many areas of physics and even more so in chemistry. The sensitivity of the nucleus to its electronic environment in a molecule (the "chemical shift") and to spin-spin interactions were originally viewed by those in the nuclear physics community as annoying features of the technique. But, the enormous potential of NMR spectroscopy for analytical studies was soon revealed through the discovery of the three peaks of ethanol in Purcell's group [27]. Almost none of the early applications of NMR were medical, although a great deal of work was published on relaxation, diffusion, and exchange of water in cells and tissues, even in living human subjects [28] and whole animals [29].

As recounted above, Magnetic Resonance Imaging came into being in 1973 with Lauterbur's publication of true 2-D NMR images (Fig. 1), reconstructed from 1-D projections acquired while magnetic field gradients were applied in various directions [1]. Soon thereafter, and quite independently, Peter Mansfield at the University of Nottingham introduced critical methods for efficient image generation, including slice selection [30] and fast "snapshot" acquisition schemes wherein entire 2-D images could be obtained in a few tens of milliseconds [31].

Recognition for key contributions

Richard R. Ernst developed Fourier transform methods that paved the way for modern MRI. He was awarded the 1991 Nobel Prize in Chemistry for "contributions to the development of the methodology of high resolution nuclear magnetic resonance (NMR) spectroscopy." Paul C. Lauterbur and Sir Peter Mansfield were then jointly awarded the 2003 Nobel Prize in Physiology or Medicine "for their discoveries concerning magnetic resonance imaging."



Reprinted with permission from The Nobel Foundation.

Another early and essential contribution to MRI was made by Richard Ernst at the Swiss Federal Institute of Technology in Zurich. During the 1960s he had introduced Fourier Transform NMR spectroscopy [32]. In 1975 he realized that one should be able to generate 2- or 3-D NMR images by applying switched magnetic field gradients as NMR signals were acquired (phase encoding), and then employing the Fourier transform methods that are now a mainstay of modern MR image reconstruction [33].

During the 1970s research in MRI was largely restricted to academic laboratories, most of them in the UK. This time period was marked by a series of important demonstrations: crude first *in vivo* images of a human finger (1975), hand (1976), thorax (1977), and head (1978). In 1980 William Edelstein, a postdoctoral fellow in John Mallard's group at the University of Aberdeen, implemented spin-warp (or Fourier) imaging and obtained the first clinically useful image of a human subject [34]. By this time, intense commercial investment in MRI had begun and clinical trials were being promoted. In 1983 Toshiba and Siemens brought the first commercial MRI scanners to market, equipped with 0.15 T (resistive) and 0.35 T (superconducting) magnets, respectively. Meanwhile General Electric, one of the current leading manufacturers, recruited several of the pioneers in the field including Edelstein. In 1985 it began to sell the first 1.5 Tesla whole-body clinical MRI system.

Over the last three decades MRI exams have become routine diagnostic procedures. In 2013, estimates place the number of operational scanners worldwide at more than 30 thousand, and the number of exams performed every year at more than 100 million (Fig. 2a; [35, 36]). The ever-growing availability and performance of these systems has facilitated a remarkable and sustained growth in applications, as evidenced by measures such as the number of publications that make reference to MRI (Fig. 2b).

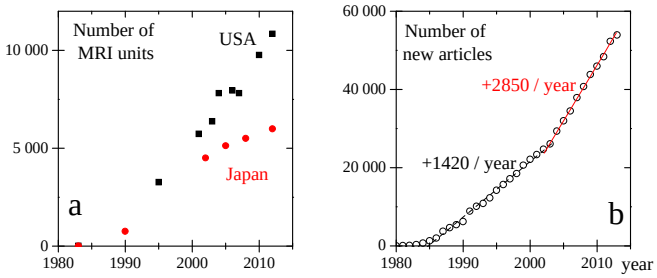


Figure 2: (a) Number of operational MRI units in two leading countries, by year [35]; (b) Number of articles published in a given year making reference to "MRI" or "MR imaging" or "magnetic resonance imaging" (Thomson Reuters *Web of Science* citation indexing service, 2014).

One of the most obvious current trends in MRI technology is a concerted move toward a large installed base of 3 T systems, particularly for neurological imaging. Some of these scanners are now even being delivered as hybrid or dual modality imaging systems, such as the promising combination of PET and MRI. There is also increasing interest in integrating the soft tissue imaging capability of MRI with interventional procedures, such as MR-guided focussed ultrasound surgery. Another significant trend is

in the area of image acquisition acceleration. The benefits of the latter include reduced motion or flow artifacts, the ability to capture anatomical motion (e.g. as desired in cardiac imaging), shorter scan times for patients, and more cost-efficient use of high demand resources. Improvements are being driven by concepts of sparse sampling (or compressed sensing) that exploit the spatial and/or temporal redundancies inherent in MRI data [37]. They are aided by parallel acquisition schemes built around the use of coil arrays, which provide direct access to spatial information and thus further enable undersampling of image data [38, 39].

Yet another promising initiative is in the area of hyperpolarization. The sensitivity of NMR as a probe is directly coupled to the orientation or alignment of nuclear spins in the applied magnetic field. At room temperature the net equilibrium alignment (or polarization) of nuclei in any laboratory field is minuscule. In 1950 Alfred Kastler predicted that this polarization could be enhanced through "optical pumping" [40]; by the 1960s this effect had been demonstrated in NMR experiments [41] and Kastler had been awarded the Nobel prize in Physics (1966) "for the discovery and development of optical methods for studying Hertzian resonances in atoms." A number of such techniques are now capable of inducing up to a million-fold increase in NMR signal strength for specific nuclei. Examples include optical pumping (OP) [41, 42], dynamic nuclear polarization(DNP) [43], and para-hydrogen induced polarization (PHIP) [44]. The enhancements provided by these methods are crucial when working with low-density or low-concentration nuclei, as encountered in MRI of gases in lung airspaces, ^{13}C nuclei in metabolites [45, 46], injected Si nanoparticles [47, 48], or "caged" ^{129}Xe [49, 50].

In retrospect, the speed and extent to which the fields of NMR and MRI evolved is remarkable. Varian Associates played a key role in the rapid transition of NMR from the laboratory to a commercial product that revolutionized chemistry. The company was incorporated in 1948 and intentionally settled near Stanford; Martin Packard, part of Bloch's team, joined shortly thereafter. From that point in time onward, technical development of the field was primarily driven by industry. Similarly in the case of MRI, as soon as the clinical potential of the technique was recognized, commercial interests drove the necessary technological developments. Throughout the 1980s a number of companies including General Electric, Picker, Toshiba, Siemens, and Hitachi, invested heavily in research and development, and promoted clinical evaluation of images. By the 1990s the installed base had grown to the point where MRI exams were commonplace in industrialized countries. To this day the number of facilities offering access to MRI continues to grow at an impressive rate while scan times get shorter and scan quality and resolution continue to increase.

It has been argued that the remarkable evolution of MRI as a clinical imaging modality benefited enormously from the timing of its invention [51]. Had the idea been proposed two decades earlier, key components of the necessary technologies would simply not have been available. In particular, the need for rapid computation of Fourier transforms would have presented an enormous challenge. On the other hand, had the idea been proposed two decades later the demand for new imaging modalities would almost certainly have been greatly reduced. By that point in time imaging modalities based on well-controlled ionizing radiation (e.g. CT-scanners) had evolved to the point where significant hurdles would have been encountered in trying to convince radiologists and medical equipment manufacturers to invest in a new and entirely unproven technology. Even more important is the extent to which the regulatory environment has changed since the 1980s. The level of proof needed to obtain safety approval is now so high that if MRI was proposed today, few if any investors would likely be willing to fund its development.

2 Fundamentals of NMR

Nuclear magnetic resonance is intrinsically a quantum mechanical phenomenon. It deals with the dynamics of microscopic objects (atomic nuclei) that behave according to the seemingly curious (but well understood) laws of quantum mechanics. Fortunately, one doesn't need years of background study in quantum mechanics in order to appreciate and understand the essential elements of MRI. The reason is that MRI is invariably used to probe macroscopic objects, involving vast numbers of atomic nuclei. The collective behaviour of these nuclei usually washes out the oddities of quantum mechanics, leaving something that bears resemblance to a familiar problem in classical mechanics: the precession of a spinning top in the earth's gravitational field. It leads to a simple but powerful mathematical description of nuclear dynamics that accurately predicts the outcome of many experiments. In this sense it often provides a sufficient basis for developing intuition and interpreting experimental results.

Unfortunately, the tendency for many people — beginners and practitioners alike — is to lose sight of the fact that the classical picture of NMR dynamics is simply an analogy: it is not a correct description of dynamics at the microscopic scale, and it can lead to nonsensical explanations of the underlying physics. Examples of situations in which the analogy has been carried too far can be found on popular websites purporting to explain NMR and MRI using pictures of toy tops or "spinning charged nuclei." As a rule of thumb, caution is advised whenever such props are encountered.

This section is organized into two parts. The first discusses the key factors that that contribute to nuclear spin dynamics, leading to a set of phenomenological equations that encapsulate the essence of the classical description of the problem. These are the famous Bloch Equations. The second part then outlines the various means by which the

practitioner interacts with the atomic nuclei in a sample, both in order to induce collective motions and to detect the resulting response.

2.1 Bloch equations and NMR dynamics

In keeping with the spirit of this book, most of this chapter makes use of the classical picture of NMR. However, in order to motivate that picture we start in section 2.1.1 with a quick glimpse at a few quantum mechanical aspects of nuclear spin dynamics. The classical treatment of the problem is then presented in section 2.1.2, leading to a statement of the Bloch Equations in section 2.1.3.

2.1.1 Spin is a quantum property

Particles such as the electron, the proton, and the neutron are characterised by their masses and electrical charges. They also possess "spin," an entirely quantum-mechanical property that is associated with an intrinsic angular momentum. (This angular momentum has nothing at all to do with physical rotation.) Spin angular momentum $\mathbf{S}$ is a vector-like quantity; it has three spatial components and can be oriented in different ways. At the same time it is different than an ordinary geometric vector. The total "amount" of spin (the length of the arrow) is fixed; it can't be changed. Moreover, only a subset of all possible orientations are permitted. More precisely, when the component S_i of angular momentum is measured in any particular direction, it is only ever observed to have discrete or "quantized" values. For a spin 1/2 particle (such as the electron, the proton, or the neutron), only two values are possible: $S_i = \pm\hbar/2$, where $\hbar$ is Planck's constant h divided by 2π. Curiously, this is less than the total spin angular momentum of the particle ($S = \sqrt{3}\hbar/2$). Pictorial representations of spins and spin states relying on arrows and cones are commonplace in MRI, but they are best viewed with caution. None of them are entirely satisfactory when held up to careful scrutiny.

Particles with spin can possess a magnetic moment $\mathbf{m} = \gamma\hbar\mathbf{S}$. Here, the constant of proportionality γ is known as the gyromagnetic ratio; each particle with a magnetic moment has a characteristic gyromagnetic ratio. Thus, even though the electron, the proton, and the neutron are all spin 1/2 particles, they have different magnetic moments (see Table 1). The same is true of strongly bound collections of particles, such as those that form the nucleus of an atom. The spins of the individual nucleons combine quantum mechanically to yield a well-defined total nuclear spin, usually denoted $\mathbf{I}$, that is characterised by its magnitude I and by a unique gyromagnetic ratio γ (Table 1). Since most applications of NMR and MRI involve nuclei with spin 1/2, this is the only case that is considered below. That being said, there are many important situations in which NMR is employed in connection with nuclei that have higher spin values; the features of the resulting spin dynamics are correspondingly more complex.

Particle or nucleus	$\gamma/2\pi$ (MHz/T)	Polarization ($\times 10^{-6}$/T)
electron	28,025	2,295
neutron	29.165	2.39
proton, ^{1}H	42.577	3.49
^{3}He	-32.434	-2.66
^{13}C	10.705	0.877
^{15}N	-4.316	-0.353
^{19}F	40.052	3.28
^{31}P	17.235	1.41
^{129}Xe	-11.777	-0.964

Table 1: Values of reduced gyromagnetic ratios $\gamma/2\pi$ and nuclear polarizations for selected spin 1/2 particles and nuclei. Equilibrium polarizations are computed for room temperature (T=293 K) using Eq. 1, and are expressed on a per unit-magnetic-field basis. Examples of nuclei with (a) Spin 0 (not suitable for NMR): ^{4}He, ^{12}C, ^{14}C, ^{16}O; (b) Spin 1: ^{2}H, ^{14}N; (c) Spin 3/2: ^{23}Na, ^{31}K; and (d) Spin 5/2: ^{17}O.

When an external magnetic field $\mathbf{B}$ is applied to a nucleus (or a particle) possessing a magnetic moment, an interaction takes place. The energy of the nucleus changes by an amount $-\mathbf{m}\cdot\mathbf{B}$, where the scalar (or dot) product "$\cdot$" accounts for the orientation of $\mathbf{m}$ relative to $\mathbf{B}$. The energy difference between the two states of the nucleus that have spin angular momentum components $\pm\hbar/2$ in the direction of $\mathbf{B}$ is $\Delta E = -\gamma\hbar B$. Peculiar features arise if the tools of quantum mechanics are brought to bear on this problem. These two particular states (often referred to as "spin-up" and "spin-down") are unique; they do not evolve in time. They are called stationary states. Other states of the nuclear spin $\mathbf{I}$ in a magnetic field are dynamic; they change as a function of time. If a weak magnetic field $\mathbf{B}_1$ is applied perpendicular to a static magnetic magnetic field $\mathbf{B}_0$ aligned with the z-axis, and B_1 is made to oscillate at an angular frequency $\omega_0 = \Delta E/\hbar = |\gamma B_0|$, the nuclear spin will execute a complex periodic oscillation back and forth between the spin-up and spin-down states via quantum superpositions of the two. If the field B_1 is eventually turned off when the nuclear spin happens to be "half-way" between the two stationary states, its transverse components I_x and I_y will continue to oscillate back and forth between their allowed values ... at the angular frequency $\omega_0 = \Delta E/\hbar = |\gamma B_0|$. The phenomenon of magnetic resonance results from the time evolution of spin states in combined static and resonantly oscillating magnetic fields.

For a physical system containing several (or many) nuclei, a full quantum treatment of spin dynamics is only required in particular situations. It is important, for instance, when short-range quantum correlations between interacting spins of nuclei in a molecule are strong. This is usually not the case in problems relevant to MRI, and a semi-classical treatment of spin dynamics is thus suffi-

cient.[1] Quantum statistical mechanics is used to evaluate the properties and time evolution of nuclear spins in a sample containing a large number of identical nuclei. Unlike individual spins that can be prepared in *pure* quantum states, a large quantum mechanical system is usually in a *mixed state*: a statistical sum of pure states in which many (or most) quantum correlations are washed out.[2] For instance, in equilibrium at a temperature T (a state known as *thermal equilibrium*) the probabilities p_{up} and p_{down} of observing the up and down states, respectively, are given by the Boltzmann factor

$$p_{\text{down}}/p_{\text{up}} = \exp(-\Delta E/k_{\text{B}}T) \ , \qquad (1)$$

where k_{B} is Boltzmann's constant. This ratio is usually very close to 1. The energy difference ΔE set by most laboratory scale magnetic fields is very small compared to the thermal energy $k_{\text{B}}T$ at room temperature, and so the probability of observing a spin in its up or down states is very nearly the same. Examples of the very small difference $p_{\text{up}} - p_{\text{down}}$, which is known as the nuclear polarization, are listed in Table 1. At the same time, the probability of observing any other spin state (i.e. in a direction tilted away from $\mathbf{B}_0$) is equal to 0: The sum $p_{\text{up}} + p_{\text{down}} = 1$.

The nuclear magnetic properties of a sample can be determined from the quantum statistical description of its spin dynamics. Each nuclear magnetic moment $\mathbf{m}$ produces a magnetic field, similar to that produced by a tiny closed loop of electric current. Technically this field is known as that of a magnetic dipole, or simply a "dipolar field." Its orientation depends on the orientation of $\mathbf{m}$ (and hence $\mathbf{I}$), and decreases rapidly in strength as one moves away from the source. Adding up contributions from many nuclei leads naturally to the concept of a local magnetization density $\mathbf{M}$, representing the magnetic moment per unit volume. The thermal equilibrium magnetization $\mathbf{M}_0$ is either parallel or antiparallel to the applied magnetic field $\mathbf{B}_0$ (depending on the sign of γ) and is proportional both to the local density of nuclear spins in the sample and to the thermal equilibrium polarization. During experiments, the nuclear magnetization can be manipulated by applying static and/or time-varying magnetic fields, as discussed below and in section 3. Similarly, the net magnetization of the sample can be inferred through monitoring the associated nuclear magnetic field. Normally this involves detecting changes in magnetic flux passing through a coil of wire (or similar structure) as the nuclear magnetization evolves in time, as discussed in section 2.2.2.

[1] A discussion of the need for a fully quantum mechanical approach to the problem can be found in [52], and references therein.

[2] Consider the following analogy to experiments with polarized light. Pure states of polarization can be combined and transformed: Right- and left-circularly polarized light can be combined to form linearly- or elliptically-polarized light. Unpolarized light, on the other hand, is different; it cannot be converted to linearly polarized light, or to any other polarized state.

Quantum dynamics of a spin 1/2 particle

The spin-up and spin-down states of a spin 1/2 particle, which are often denoted $|+\rangle$ and $|-\rangle$, are called pure states. Repeated measurements of their spin angular momentum along a particular axis (as was done in the Stern-Gerlach experiment mentioned in section 1) always yield $\hbar/2$ for the up state and $-\hbar/2$ for the down state. All other pure states, with a maximum spin projection value $\hbar/2$ in a direction $\hat{u}$ other than $\pm$z, are "linear superpositions" of these states: $\alpha\,|+\rangle + \beta\,|-\rangle$, where α and β are complex coefficients such that $\alpha^2 + \beta^2 = 1$. For instance, $(|+\rangle + |-\rangle)/\sqrt{2}$ is the pure state in the $\hat{x}$ direction, and $(|+\rangle + i\,|-\rangle)/\sqrt{2}$ is the pure state in the $\hat{y}$ direction. Unlike the up and down states, these quantum mechanical superpositions are not stationary; they evolve in time. In particular, the direction $\hat{u}$ evolves in exactly the manner predicted by the semi-classical treatment of the time evolution of $\mathbf{m}$ summarized in section 2.1.2.
These concepts can be extended. For example, a two level atomic system is formally identical to a spin 1/2 quantum system. Transitions between the two (quasi-) stationary states of the atom correspond to the emission or the absorption of a quantum of energy (a photon). This picture forms the basis for the popular – but incorrect – statement that NMR phenomena involve the emission or absorption of radio waves. To understand why this statement is wrong, one need only consider the fact that the electromagnetic wavelength associated with the Larmor frequency produced by a laboratory strength magnetic field is almost always large compared to the dimensions of typical samples and receive coils. In other words, NMR (and particularly MRI) is performed in the near-field electromagnetic regime and the photons that are involved are virtual [53, 54].

2.1.2 Classical magnetization dynamics

A classical description of nuclear spin dynamics is obtained by considering a model system in which the macroscopic magnetic moment $\mathbf{m}$ and resultant angular momentum $\mathbf{J}$ are coupled such that $\mathbf{m} = \gamma\mathbf{J}$. This seemingly innocuous relationship is the same as that which is obeyed by individual nuclei, only now $\mathbf{m}$ and $\mathbf{J}$ are purely classical quantities (not subject to the subtle restrictions imposed by quantum mechanics). This vector proportionality causes a gyroscopic response to an applied magnetic field, analogous to the dynamics of a spinning top in a gravitational field.

A misleading analogy: the compass needle

The relationship $\mathbf{m} = \gamma\mathbf{J}$ is not a general property of macroscopic objects. The magnetic moment of a compass, for example, is locked to the long axis of the needle, which is in turn free to rotate in a plane about its midpoint. (This is what makes the compass a useful device.) The angular momentum of the compass, on the other hand, is proportional to the angular rotation rate of the needle. Thus, $\mathbf{m} \neq \gamma\mathbf{J}$. A compass needle oscillates in a plane about its midpoint; it does not precess like a spinning top or like a collection of nuclear spins! Conversely, the nuclear magnetization in NMR is not locked to the physical orientation of the sample (or subject), as is the magnetization of a compass needle. Thus, in *magic angle spinning* (MAS; an NMR technique in which the sample is physically rotated at high speed) it is the lattice of the crystal structure that is spun, not the nuclear magnetization.

In a sample or subject, the local macroscopic magnetization density $\mathbf{M}$ associated with the magnetic moments of the nuclei obeys the classical equation of motion:

$$\frac{d\mathbf{M}}{dt} = \gamma\mathbf{M} \times \mathbf{B} \ . \qquad (2)$$

An important feature of this equation is that the amplitude M of the local magnetization (the length of the vector $\mathbf{M}$) remains constant. At all times the change in $\mathbf{M}$ is perpendicular to both $\mathbf{M}$ and $\mathbf{B}$. This behaviour is encoded in the vector (or cross) product "$\times$" in Eq. 2.

A common and convenient graphical tool for depicting the time evolution of $\mathbf{M}$ is the *Bloch sphere*: an imaginary sphere of radius M. With a coordinate system chosen such that the static magnetic field $\mathbf{B}_0$ is aligned with the z axis, the corresponding thermal equilibrium magnetization $\mathbf{M}_0$ can be drawn as a vector pointing from the midpoint of the sphere to the "North Pole." In this case $\mathbf{M} = \mathbf{M}_0$ and $\mathbf{B} = \mathbf{B}_0$, and so Eq. 2 gives $d\mathbf{M}/dt = 0$. That is, nothing happens; $\mathbf{M}$ remains aligned with $\mathbf{B}_0$. The same thing is true if $\mathbf{M}$ is somehow aligned to point to the"South Pole" of the Bloch sphere. In the language of section 2.1.1, these situations correspond to the two stationary quantum spin states.

If instead $\mathbf{M}$ is somehow reoriented so that it is canted with respect to $\mathbf{B}_0$ by some angle other than 180°, as shown in Fig. 3, Eq. 2 gives a non-zero result for $d\mathbf{M}/dt$. In this case the tip of the magnetization vector traces out a circular path at constant latitude, returning periodically to its starting point. This motion is referred to as *free precession*. Unless other processes intervene, it persists forever. It occurs at an angular velocity

$$\boldsymbol{\Omega}_0 = -\gamma\mathbf{B}_0 \qquad (3)$$

or angular speed $\Omega_0 = -\gamma B_0$, both of which indicate the sense of the motion. The expression *angular Larmor frequency* is used by some authors to describe Ω_0 while others take it to mean $\omega_0 = |\gamma B_0|$. Care is thus required any time the absolute sense of rotation is needed. Importantly, the Larmor frequency is independent of the angle to which $\mathbf{M}$ is canted relative to $\mathbf{B}_0$.

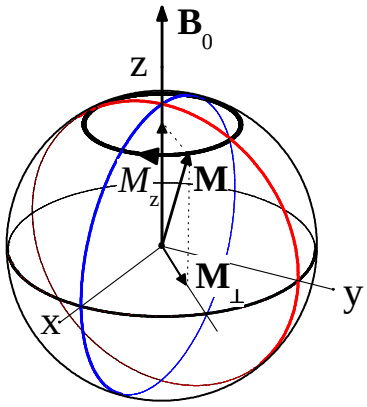


Figure 3: Graphical representation of solutions to Eq. 2, for a constant field $\mathbf{B}_0$. The time-dependent magnetization vector $\mathbf{M}$ can be associated with a point on a sphere of radius M centred at the origin: the Bloch sphere. The longitudinal component M_z of $\mathbf{M}$ is static, while the transverse component $\mathbf{M}_\perp$ rotates in the transverse (xy) plane at the angular Larmor frequency ω_0.

The phenomenon of nuclear magnetic resonance enters when a time varying magnetic field $\mathbf{B}_1$ is added. Imagine that a weak magnetic field $\mathbf{B}_1$ is added perpendicular to the static field $\mathbf{B}_0$, and that $\mathbf{B}_1$ rotates about $\mathbf{B}_0$ at the Larmor frequency. That is, the amplitude of $\mathbf{B}_1$ is constant while its direction changes. In this case $\mathbf{M}$ must precess about both $\mathbf{B}_0$ and $\mathbf{B}_1$, and so the tip of the vector traces out two simultaneous motions: a fast precession about $\mathbf{B}_0$ and a slow precession about the instantaneous orientation of $\mathbf{B}_1$. This produces tightly wound spiral trajectories such as the one shown in Fig. 4a.

The examples shown in Figs. 3 and 4a reveal that the longitudinal and transverse components of $\mathbf{M}$ exhibit very different dynamical behaviour. The dynamics of the longitudinal component M_z (a scalar) correspond to a slow oscillation that involves variations in amplitude. The dynamics of the transverse component $\mathbf{M}_\perp$ (a 2-D vector), on the other hand, involve a fast rotation about the z axis at angular frequency ω_0 combined with a slow oscillation that involves variations in amplitude. Here $\mathbf{M}_\perp$ can be decomposed into orthogonal components M_x and M_y. Equivalently it can be represented as the quantity $M_x + iM_y$ in the complex plane. The latter approach enables one to use complex algebra rather than matrix algebra in the solution of Eq. 2. With complex algebra, a rotation of the complex quantity $\mathbf{M}_\perp$ by an angle Φ is obtained by adding Φ to its phase, or multiplying by $e^{i\Phi}$.

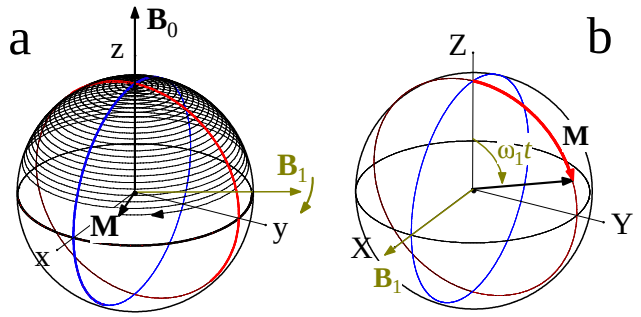


Figure 4: (a) Part of the spiral trajectory executed by the tip of the magnetization vector under resonance conditions. It results from the cumulative action of a weak magnetic field $\mathbf{B}_1$ in the xy plane, rotating at the angular Larmor frequency ω_0. The amplitudes of the longitudinal (M_z) and transverse ($\mathbf{M}_\perp$) components of $\mathbf{M}$ oscillate periodically. (b) The same trajectory is shown in the rotating frame where $\mathbf{B}_1$ is fixed along the X-axis (see text).

Setting $\mathbf{B} = \mathbf{B}_0$ and using complex notation for $\mathbf{M}_\perp$ reduces Eq. 2 to $d\mathbf{M}/dt = -i\gamma B_0 \mathbf{M}_\perp$. The solution to this differential equation is the trajectory shown in Fig. 3: that is, M_z is constant and $\mathbf{M}_\perp(t) = \mathbf{M}_\perp(0)e^{i\Omega_0 t}$ where $\Omega_0 = -\gamma B_0$. Note here that the sense in which the tip of the vector $\mathbf{M}$ traces out a circle depends on the sign of γ. When $\gamma > 0$ and the Bloch sphere is viewed from above, the sense of the free precession trajectory is clockwise. If $\gamma < 0$, as it is for some of the nuclei listed in Table 1, the sense of the free precession trajectory is counter-clockwise. The sense of this rotation can be assessed experimentally by using two orthogonal detectors; the phase difference between the signals induced in the two detectors reveals the sense of the trajectory and hence the sign of γ.

The motion of $\mathbf{M}$ is complicated by the rapid rotation of $\mathbf{M}_\perp$ about $\mathbf{B}_0$ at the Larmor frequency. It is technically simpler to display and compute trajectories of $\mathbf{M}$ if one works in a reference frame that is also rotating about the z axis at the Larmor frequency. This is analogous to jumping onto a merry-go-round (or carousel) to better observe the wooden horses and their riders. More precisely, in a reference frame with axes X, Y, and Z rotating at angular velocity $\mathbf{\Omega}$ about the Z-axis (with Z ≡ z), Eq. 2 becomes:

$$\begin{aligned}\frac{d\mathbf{M}}{dt} &= \gamma\mathbf{M}\times\mathbf{B}_0 + \mathbf{M}\times\mathbf{\Omega} \\ &= \gamma\mathbf{M}\times\left(\mathbf{B}_0 + \frac{\mathbf{\Omega}_0}{\gamma}\right) \end{aligned} \quad (4)$$

where $\mathbf{B}$ has been set to $\mathbf{B}_0$. Comparison of Eqs. 2 and 4 reveals that the magnetization now behaves as if it is responding to an apparent field

$$\mathbf{B}_{\rm app} = \mathbf{B}_0 + \mathbf{\Omega}/\gamma, \quad (5)$$

and that in this frame its angular velocity is $\mathbf{\Omega}_0 - \mathbf{\Omega}$. If the rotation rate is chosen such that $\mathbf{\Omega} = \mathbf{\Omega}_0$, the apparent magnetic field $\mathbf{B}_{\rm app}$ vanishes and the magnetization vector $\mathbf{M}$ appears stationary.

Likewise, when a transverse magnetic field $\mathbf{B}_1$ rotating about $\mathbf{B}_0$ is added, the time evolution of $\mathbf{M}$ is best described using a reference frame in which $\mathbf{B}_1$ appears stationary. That is, in a reference frame that is synchronous with $\mathbf{B}_1$. In any such frame Eq. 2 becomes:

$$\frac{d\mathbf{M}}{dt} = \gamma\mathbf{M}\times(\mathbf{B}_{\rm app}+\mathbf{B}_1)\ . \quad (6)$$

If the field $\mathbf{B}_1$ is resonant with the free Larmor precession of the magnetization (i.e., $\mathbf{\Omega} = \mathbf{\Omega}_0$ so that $\mathbf{B}_{\rm app} = 0$), then $\mathbf{M}$ simply rotates around $\mathbf{B}_1$ at an angular velocity $\mathbf{\Omega}_1 = -\gamma\mathbf{B}_1$ and its tip traces out a great circle on the Bloch sphere. This scenario is sketched in Fig. 4b, where the particular rotating frame that was chosen is the one in which $\mathbf{B}_1$ is aligned with the X axis. Viewed in the laboratory frame, this motion produces the spiral trajectory shown in Fig. 4a. The pitch of the spiral is given by the ratio of magnetic field amplitudes B_1/B_0.

This last example forms the basis for pulsed NMR. If the field $\mathbf{B}_1$ is applied on resonance for a finite period of time τ, $\mathbf{M}$ traces out an arc on the surface of the Bloch sphere that subtends an angle $\theta = \omega_1\tau$. Afterward, $\mathbf{M}$ undergoes free precession as shown in Fig. 3. Here $\omega_1 = |\Omega_1|$ denotes the angular nutation frequency and the finite-duration $\mathbf{B}_1$ field is referred to as a tipping pulse. The angle θ through which $\mathbf{M}$ is rotated is variously referred to as the tip, flip, rotation, or nutation angle. It can be controlled through the amplitude of B_1 or the time τ. Starting from thermal equilibrium where $\mathbf{M} = \mathbf{M}_0$, a 90° or $\pi/2$ tipping pulse will rotate the magnetization into the transverse plane, at which point it will undergo free precession. Alternately, a 180° or π pulse will invert the magnetization, transforming it from $\mathbf{M}_0$ to $-\mathbf{M}_0$.

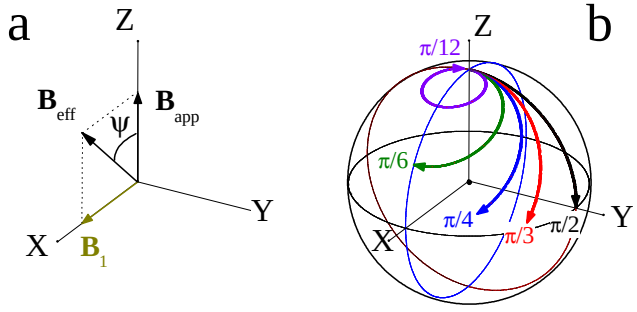


Figure 5: (a) Components $\mathbf{B}_1$ and $\mathbf{B}_{\rm app}$ of the effective magnetic field $\mathbf{B}_{\rm eff}$, in the rotating frame. (b) Examples of trajectories on the Bloch sphere for several detunings. In each case the same evolution time $\tau = \pi/2\Omega_1$ is employed. Values of the angle ψ, which characterize the extent of the detuning (i.e., $\tan\psi = \Omega_1/|\Omega - \Omega_0|$) are indicated.

If the field $\mathbf{B}_1$ is applied off resonance rather than precisely at the Larmor frequency, it is still convenient to work in a frame that is synchronous with $\mathbf{B}_1$ and employ

Eq. 6. The magnetization now rotates around an effective field $\mathbf{B}_{\text{eff}} = \mathbf{B}_{\text{app}} + \mathbf{B}_1$ as shown in Fig. 5a, and the trajectories traced out by the tip of $\mathbf{M}$ are no longer great circles. If one starts from an initial magnetization $\mathbf{M}_0$ aligned with $\mathbf{B}_0$ it is no longer possible to reach the antipodal point on the Bloch sphere where $\mathbf{M} = -\mathbf{M}_0$; that is, perfect π-pulses leading to magnetization reversal are only possible at resonance. As the detuning $|\Omega - \Omega_0|$ increases, the circular trajectories traced by the tip of $\mathbf{M}_0$ on the Bloch sphere (in the rotating frame) become smaller and they are travelled at faster rates (Fig. 5b). This illustrates the fact that NMR tipping pulses are frequency-selective. Only spins that precess at frequencies close to that of the applied $\mathbf{B}_1$ field are influenced to any significant degree.

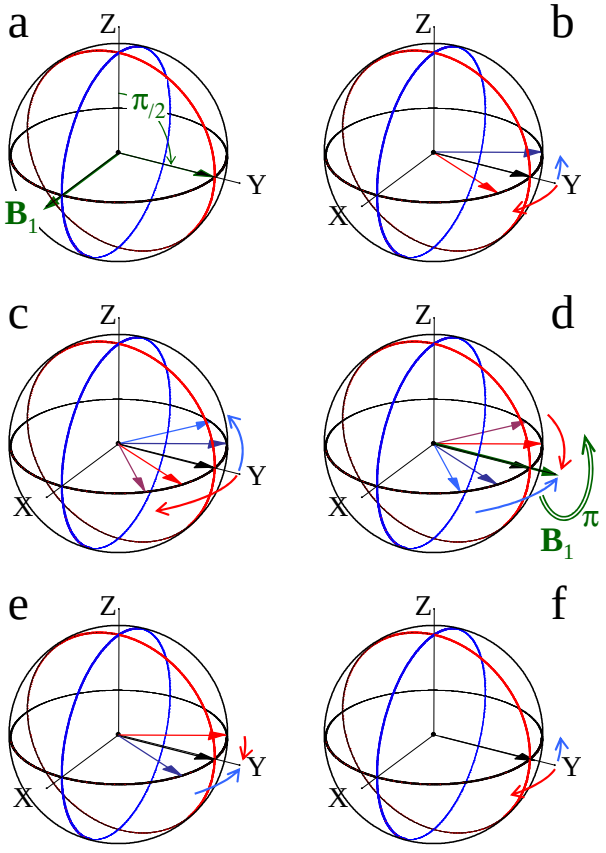


Figure 6: Spin dephasing and echo formation in the rotating frame: (a) A $\pi/2$ tipping pulse rotates the thermal equilibrium magnetization into the transverse plane. Over time (b-c) some spins precess faster than average while others precess slower. A distribution of azimuthal angles builds up, represented schematically by arrows indicating isochromats. (d) A π pulse applied along the Y axis when the distribution is as shown in (c) inverts the magnetization. Over time (e-f) the magnetization is refocussed, leading to a revival (spin-echo) in panel (f). At times later than those shown here the spins continue to dephase.

As another example, consider situations where the Larmor precession frequency is not the same for all nuclei in a sample. This inhomogeneity could be the result of an intentionally applied magnetic field gradient, or it could be the result of an intrinsic property of the sample. In either case there is no unique rotating reference frame in which $\mathbf{B}_{\text{eff}}=0$ everywhere. Despite this, it is still advantageous to work in a rotating reference frame, a common choice being a frame that rotates at the average Larmor frequency. Figure 6 shows a sequence in which (a) a $\pi/2$ pulse is used to rotate the thermal equilibrium magnetization $\mathbf{M}_0$ into the transverse plane, at which point (b-c) the magnetization undergoes free precession. Unlike the situation pictured in Fig. 3, the Larmor precession rate is not uniform; some spins precess faster than the average rate and some spins precess slower. This distribution is shown schematically as a series of arrows representing "isochromats": idealized collections of spins that precess at the same rate. Over time the distribution of angles subtended by these isochromats grows and the net transverse magnetization diminishes. If the sequence pictured in panels (b) and (c) of Fig. 3 is allowed to continue indefinitely, the net transverse magnetization will average to zero.

Hahn recognized that the ordered dephasing of isochromats evident in Fig. 6 can be "undone" by applying another tipping pulse, leading to the formation of a spin-echo (or a Hahn-echo) [26]. For example, if a π pulse at the average Larmor frequency is applied along the Y axis at the time pictured in panel (c) of Fig. 6, the isochromats undergo a 180° rotation. Thus in panel (d) the isochromats that precess at the fastest rate are behind the average in terms of total accumulated phase. Conversely, the isochromats that precess at the slowest rate are ahead of the average. As the magnetization continues to execute free precession the angular width of the distribution narrows, forming a revival or spin echo in panel (f).

2.1.3 Irreversibility: the Bloch Equations

The classical theory of nuclear spin dynamics summarized above provides tools for manipulating nuclear spins, and for establishing states characterized by various forms of phase coherence (or correlation) between local magnetization vectors. These states do not persist forever. Given enough time, and the absence of further manipulations, we expect any interacting spin system to return to thermal equilibrium. That is, a state where $\mathbf{M}$ is aligned with $\mathbf{B}_0$ and has a magnitude M_0 that is set by the Boltzmann distribution (Eq. 1).

The processes through which a spin system returns to thermal equilibrium can be complex. They typically involve an exchange of energy between the spins and their environment, and are usually mediated by random magnetic interactions. In many practical circumstances the rate at which this exchange proceeds can be characterized by a phenomenological time scale referred to as the "spin-lattice relaxation time" or the "longitudinal relax-

ation time." By convention it is designated by the symbol T_1. If the longitudinal component of $\mathbf{M}$ is displaced from thermal equilibrium, the equation of motion governing its return is

$$\frac{dM_z}{dt} = -\frac{(M_z - M_0)}{T_1} . \quad (7)$$

Thus, if $\mathbf{M}_0$ is inverted at time $t = 0$ through application of a π pulse, the return of M_z to equilibrium is given by

$$M_z(t) = M_0 [1 - 2\exp(-t/T_1)] . \quad (8)$$

Similarly, coherence of the local transverse magnetization is degraded over time by random interactions or processes that destroy correlations. This degradation is distinct from the dephasing of spins in an inhomogeneous magnetic field described in connection with Fig. 6, in the sense that it is irreversible. No subsequent manipulation of the nuclear spins can produce an echo or revival. Again, in many practical circumstances the rate at which coherences of the transverse magnetization are attenuated can be characterized by a phenomenological time scale referred to as the "spin-spin relaxation time" or the "transverse relaxation time." By convention, it is designated by the symbol T_2. If the magnetization is manipulated so as to establish a transverse component, and then allowed to undergo free precession, the equation of motion describing the inevitable attenuation of $M_\perp$ is

$$\frac{\mathbf{M}_\perp}{dt} = -\frac{\mathbf{M}_\perp}{T_2} . \quad (9)$$

Thus if a $\pi/2$ pulse is applied to a spin system in thermal equilibrium, producing $M_\perp = M_0$ at time $t = 0$, the transverse magnetization subsequently satisfies

$$M_\perp(t) = M_0 \exp(-t/T_2) . \quad (10)$$

The full equations of motion for the local magnetization density $\mathbf{M}$ that give rise to these exponential relaxation functions are known as the Bloch Equations. They can be written

$$\frac{d\mathbf{M}}{dt} = \gamma \mathbf{M} \times \mathbf{B} - \frac{\mathbf{M}_\perp}{T_2} - \frac{(M_z - M_0)}{T_1} \quad (11)$$

where the first term on the right accounts for precession and the other terms account for relaxation. A more compact expression is obtained by introducing the relaxation matrix

$$[R] = \begin{pmatrix} 1/T_2 & 0 & 0 \\ 0 & 1/T_2 & 0 \\ 0 & 0 & 1/T_1 \end{pmatrix} \quad (12)$$

and writing

$$\frac{d\mathbf{M}}{dt} = \gamma \mathbf{M} \times \mathbf{B} + [R](\mathbf{M}_0 - \mathbf{M}) . \quad (13)$$

Even though the original formulation of these equations was based on two phenomenological parameters, there are many important situations in which T_1 and T_2 can be derived from quantum mechanical principles.

Origin and regimes of relaxation

In liquids and gases, rapid random fluctuations of intermolecular orientations and distances permit the use of perturbative methods to evaluate relaxation. This was originally described by Bloembergen, Purcell, and Pound and has since often been called the BPP theory [55]. A key parameter in this theory is the correlation time, τ_c, which characterizes the relevant fluctuations in the relaxation process. An important result of the BPP theory is that it predicts exponential relaxation for both M_z and $M_\perp$, and provides values for the corresponding relaxation time constants T_1 and T_2. In the weak field - fast motion limit ($\omega_0\tau_c \ll 1$), T_1 and T_2 are equal and proportional to $1/(\omega_0\tau_c)$. In the opposite high field - slow motion regime, $T_2 \propto 1/(\omega_0\tau_c) \ll T_1 \propto \omega_0\tau_c$. A minimum in T_1 is obtained in the intermediate regime, for $\omega_0\tau_c = 1$. Over the years, more elaborate descriptions have been developed, encompassing different situations of interest in NMR spectroscopy [56] but seldom relevant for MRI of tissues.

Examples illustrating the combined influence of T_1 and T_2 on the time evolution of $\mathbf{M}$ are shown in Fig. 7. One of the most striking differences relative to examples in the previous section is that the trajectory of the tip of $\mathbf{M}$ is no longer restricted to the surface of the Bloch sphere. In panel (a) of Fig. 7, T_2 is substantially shorter than T_1. The resulting spiral collapses toward the z-axis much faster than it climbs toward the North pole. In panel (b) the two relaxation times are equal. In this case the spiral trajectory is constrained to a cone-like surface. Panel (c) shows the recovery of the longitudinal magnetization M_z and the decay of the transverse magnetization $M_\perp$ for both scenarios. Note that the timescale has been normalized to T_1 and so the recovery of M_z is the same for both cases. Finally, the decays of $M_\perp$ are shown again in panel (d), in order highlight the fact that they are exponential.

One often encounters situations where the Bloch equations alone are not sufficient to characterize the time evolution of $\mathbf{M}$. Random atomic or molecular motions, for example, bring in the irreversible effects of diffusion. For liquids and gases these effects can often be characterized in terms of a diffusion coefficient D. More generally, when anisotropic media such as nerve tissue are involved, Eq. 13 becomes

$$\frac{d\mathbf{M}}{dt} = \gamma \mathbf{M} \times \mathbf{B} + [R](\mathbf{M}_0 - \mathbf{M}) - \nabla \cdot [D] \nabla M \quad (14)$$

where $[D]$ is the diffusion tensor. Equation 14 is known as the Bloch-Torry equation [57]. It provides the basis for extracting information about diffusion from NMR experiments, and is central to understanding diffusion-weighted and diffusion-tensor MRI.

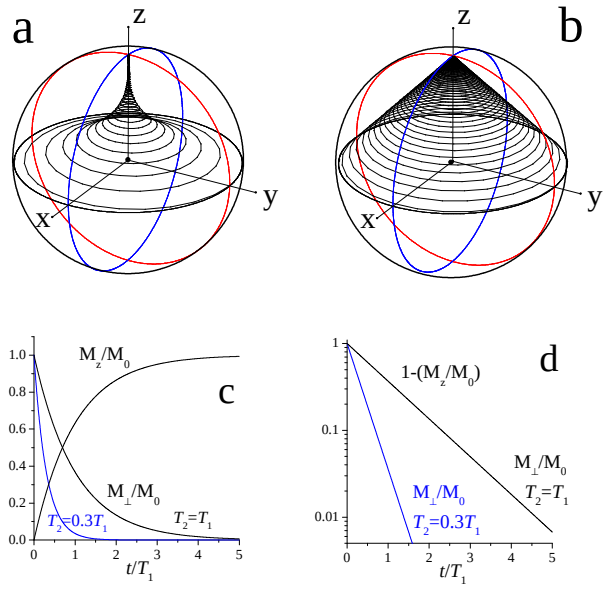


Figure 7: Influence of relaxation on the time evolution of **M**. Trajectories are shown for an initial transverse magnetization aligned with the y axis, for (a) $T_2 = 0.3T_1$ and (b) $T_2 = T_1$. Panel (c) shows the normalized magnitudes of M_z and $M_\perp$. Panel (d) shows the normalized magnitude of $M_\perp$ again, on a logarithmic scale.

2.2 Electrodynamics of NMR

A myriad of magnetic resonance imaging sequences exist, but they all start with the preparation of atomic nuclei in some well-defined state other than thermal equilibrium. They all also involve a mapping of the local Larmor precession frequency onto position. Information about the spatial distribution of some aspect of the nuclear magnetization **M** (such as the number of contributing nuclei, their local environment, or their displacement over time) is then inferred through monitoring the transverse component of **M** (*i.e.* $\mathbf{M}_\perp$) as it evolves in time (and ultimately relaxes toward thermal equilibrium). A complete image is built up by repeating this measurement over and over again, as the mapping is systematically varied over an appropriate range of parameters.

The general procedures alluded to above are discussed further in section 3. Before getting to that point, however, it is worth examining the methods by which nuclear spin dynamics are initiated and manipulated. This is the focus of section 2.2.1. It is also useful to understand the methods used to monitor nuclear spin precession. This is covered in section 2.2.2. In both cases the discussion is limited to the basic physics that is involved, as opposed to the instrumentation that is employed. Next, in order to set the stage for a discussion of specific imaging sequences, it is helpful to examine factors that influence the amplitude of signals that are detected in MRI, and the extent to which these signals are influenced by unavoidable (intrinsic) sources of noise. This is the topic of section 2.2.3. Finally, some of the same physics that is wrapped up in signal detection is responsible for undesirable effects: the deposition of radiofrequency energy into the subject and peripheral nerve stimulation. These issues are briefly summarized in section 2.2.4.

2.2.1 Ampère's Law: Currents, coils and fields

The dynamics of nuclear spin precession are controlled during MRI sequences by imposing magnetic fields. These magnetic fields are in turn produced by electric currents, and in some cases by magnetized (and/or magnetizable) materials. The precise manner in which magnetic fields are generated and influenced by these currents and magnetic materials is encapsulated in a mathematical expression known as Ampère's Law.[3] The various fields that are typically required for MRI are summarized below.

Static Field

A magnetic field is required to establish an energy difference between the spin-up and the spin-down states of the nucleus (section 2.1.1). This is done by immersing the subject in a homogeneous magnetic field $\mathbf{B}_0$. This field is variously referred to as the static field, the main field, the homogeneous field, or simply "Bee-zero" or "Bee-naught."It is conventional to choose the direction of $\mathbf{B}_0$ as the direction that defines the z-axis of the coordinate system.

The simplest and most effective way to produce a strong, homogeneous, and accessible magnetic field is with a solenoid: a single wire wrapped many times around the circumference of a cylinder. When current flows through the wire, a homogeneous magnetic field is produced along the axis of the cylinder.[4] The central field produced by a thin uniformly wound cylindrical solenoid of length L and diameter D such as the one shown schematically in Fig. 8 is given by

$$B_0 = \frac{\mu_0 n I}{\sqrt{1 + (D/L)^2}} \tag{15}$$

where $\mu_0 = 4\pi \times 10^{-7}$ Tm/A is the permeability of free space and n represents the winding density. Choosing $L = 1.8$ metres, $D = 0.9$ metres, $I = 190$ Amperes, and $n = 7 \times 10^3$ turns per metre (*i.e.* a wire wrapped around the cylinder approximately 12,600 times, for a length totalling a few tens of km) yields $B = 1.5$ Tesla, which is typical of the fields employed in the majority of clinical imagers in service today.[5] In practice superconducting solenoids are usually employed to generate this magnetic field. These "magnets" are operated in a "persistent" mode at cryogenic temperatures such that current flows through the solenoid in a closed loop, without

[3] Additional considerations come into play when high frequencies are involved. In such cases, Maxwell's Equations (which include the physics described by Ampère's Law) are employed.

[4] The field is perfectly homogeneous only for an infinitely long solenoid.

[5] To put this in perspective, the Earth's magnetic field is of order 10^{-4} Tesla or 1 Gauss.

a power supply and effectively without dissipation. The main field magnet and the associated cryogenic vessel account for the bulk of the tube-like infrastructure that one normally sees when looking at an MRI scanner.

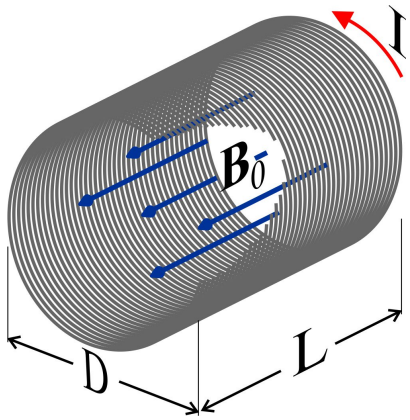


Figure 8: A solenoid of length L and diameter D carrying current I. The central magnetic field B_0 is given by Eq. 15. The large number of turns required for an MRI magnet results in a coil that has many layers. Normally the winding density is varied to improve the field homogeneity. A second (larger) solenoid wound outside the primary magnet, and in the opposite sense, provides "active shielding." The net field at the centre of the combined magnet is somewhat weaker than that of primary magnet alone, but the external field is dramatically suppressed.

A key function of the main magnetic field is to set a uniform Larmor precession frequency for all of the nuclei that are going to be imaged.[6] In practice a simple finite length solenoid (or other winding pattern, or other magnet geometry) is not sufficient to produce the native magnetic field homogeneity that is required for high resolution MRI. A number of shim (or correction) coils and judiciously placed ferromagnetic (magnetizable) materials are also used to create a central volume over which a very high degree of magnetic field uniformity (and hence nuclear spin precession rate) are achieved. The subject is then positioned such that the region to be imaged coincides with this "sweet spot." In typical whole body clinical MRI systems B_0 varies by at most a few parts-per-million over a 30 cm diameter sphere at the centre of the magnet (distortions equivalent to adding or subtracting a fraction of the Earth's magnetic field to B_0).

The nominal Larmor precession rate for ^{1}H nuclei (protons) in a 1.5 Tesla imager is 63.87 MHz (cf. Table 1). In a 3 Tesla imager it is 127.73 MHz. Yet higher static magnetic fields can and have been employed for MRI, and yield substantial improvements in signal-to-noise ratio (SNR).[7]

[6] It is also usually responsible for establishing the thermal equilibrium polarization of the nuclei, and hence the maximum amplitude of the signals that can be detected.

[7] They also present new challenges, such as limitations on the amplitude and duration of radiofrequency pulses that can be applied, as discussed in sections 2.2.2 and 2.2.4.

Range	Field Strength (Tesla)	^{1}H frequency (MHz)
High	$B_0 > 2$	$f > 85$
Conventional	$0.5 < B_0 < 2$	$20 < f < 85$
Low	$0.1 < B_0 < 0.5$	$4 < f < 20$
Very-Low	$0.001 < B_0 < 0.1$	$0.04 < f < 4$
Ultra-Low	$B_0 < 0.001$	$f < 0.04$

Table 2: Classification of MRI scanners by static field strength. Over time the definition of what constitutes a "high field" system has drifted upward. During the 1980s a 1 T scanner would have been considered a high-field system. Most clinical systems in service today operate at 1.5 T, but the fastest growing segment of the market is for 3 T systems. The production of low-field scanners has dropped significantly in recent years. Scanners that operate in the very-low and ultra-low regimes are employed for niche applications.

Lower fields can also be employed, and offer other advantages such as the possibility open geometries where ready access to the subject is possible and the imager environment is less likely be claustrophobic. The magnets at the heart of these low-field systems can be wound from superconducting wire or ordinary copper wire, or they can be constructed from permanent magnets. Imagers that operate at yet lower magnetic fields have been developed in connection with a variety of different research initiatives. A crude classification of MR imagers by magnetic field strength is given in Table 2.

Gradient Fields

Spatial resolution in MRI is accomplished by inducing well defined distortions of the main magnetic field, which produce the desired mapping between nuclear precession frequency and position. These distortions are created by running currents through sets of coils that are designed for this purpose.[8] This is precisely what Lauterbur did in his original demonstration (Fig. 1). It is conventional to refer to these distortions as magnetic field gradients, and to the coils that produce them as gradient coils.

In a solenoidal main-field geometry, a longitudinal field gradient $G_z = dB_z/dz$ increases the field strength toward one end of the cylinder and decreases it toward the other. Transverse gradients ($G_x = dB_z/dx$ and $G_y = dB_z/dy$) increase the field strength on one side of the cylinder and decrease it on the other (to the left and the right of the subject, or above and below, or in fact in any transverse direction that is desired). Simple sets of coils generating such field gradients are sketched in Fig 9. Improved per-

[8] Large magnetostatic forces are exerted on these coils whenever current flows through them. Imaging sequences normally require rapid switching or pulsing of the field distortions. The sudden changes in mechanical stress exerted on the coil support structure produces the characteristic patterns of acoustic noise that are generated by MRI scanners.

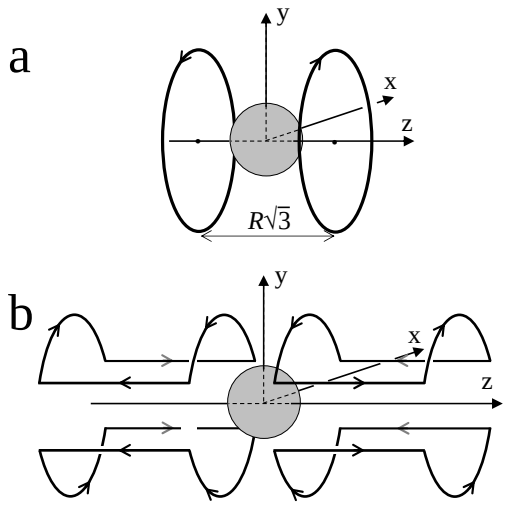


Figure 9: Elementary coil winding patterns that generate field gradients over a central region (indicated by the grey sphere). The main magnetic field B_0 is assumed to be in the $\hat{z}$ direction. (a) A Maxwell coil pair, with currents flowing in opposite directions, creates a z-odd field variation and hence produces a longitudinal gradient G_z. For the specified coil spacing, the z^3 term in the series expansion of the field vanishes, and G_z has a high uniformity. (b) A Golay coil consists of four saddle coils with currents flowing in the specified directions. It produces a transverse gradient G_y. Current flowing in the wires parallel to the z axis does not produce a field in the $\hat{z}$ direction and does not affect G_y. The positions of the arcs and the angle that they subtend are chosen so as to maximise gradient uniformity. Note that the orientation of the x, y, and z axes differs from that chosen in the previous section: the z-axis is still aligned with B_0, but is is now shown as being horizontal as it is for almost all clinical MRI systems.

formance is obtained using analytical or numerical methods to obtain complex yet compact winding patterns for which gradient strengths and uniformity are maximized and the associated coil inductance is minimized [58, 59].

Normally the field distortions induced by gradient coils are very small. For example, at 1.5 Tesla they are typically less than 1% of B_0 over the Field of View (FOV). A careful examination of the magnetic fields produced by gradient coils reveals that they always do more than simply provide the nominal "desired effect." For example, a coil that produces a longitudinal field gradient dB_z/dz always produces a gradient in orthogonal components of the field (dB_x/dx and/or dB_y/dy).[9] In many instances the effects produced by these "concomitant gradients" (or Maxwell terms) is negligible, simply because the magnitude of the transverse components of the distorted field (B_x and B_y) are so small compared to the longitudinal field B_0. But, this is not always the case, particularly when very strong gradients or weak static fields are employed.

[9]The term field gradient, which is ubiquitous in MRI, is really a misnomer. It is technically a tensor quantity with 9 components. In free space, constraints imposed by Maxwell's equations reduce the number of independent terms in the tensor to 5.

RF Field

Up to this point all of the coils that have been discussed serve to control and manipulate the longitudinal magnetic field B_z, and hence the Larmor precession frequency. They do not produce fields that induce transitions between nuclear energy levels. For this one usually needs a field directed orthogonal to B_z that oscillates at the Larmor frequency, or close to it. That is, the field B_1 of section 2.1.2 which causes the net nuclear magnetization $\mathbf{M}$ to rotate about an axis perpendicular to z, as long as it is applied.

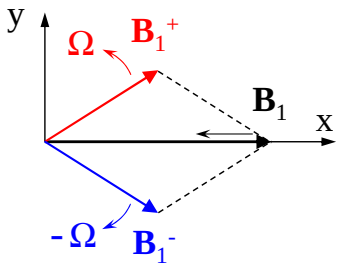


Figure 10: A linearly-polarized oscillating magnetic field $B_1(t) = B_1^{\mathrm{m}} \cos \Omega t$ aligned with the x-axis can be decomposed into two rotating components with equal and constant amplitudes but opposite angular velocities. That is, $B_1(t) = (B_1^{\mathrm{m}}/2)\left[\exp(i\Omega t) + \exp(-i\Omega t)\right]$.

In practice, the rotating field B_1 is often obtained as one of the two counter-rotating components of a linearly-polarized oscillating field (see Fig. 10). The other component, which rotates in the opposite sense, is detuned from the nuclear resonance by twice the Larmor frequency. It thus has almost no effect on nuclear spin dynamics. This linearly-polarized oscillating field is produced by driving a time-varying current $i_0 \cos \Omega t$ through a coil with an appropriate geometry. The amplitude of this current (and hence the amplitude of the field B_1) and time period over which it is applied control the tip (or flip) angle. Dozens of such coils have been developed and employed for MRI; they are generically known as transmit coils (or antennas), TX coils, radiofrequency (or "RF") coils, or even B_1 coils ("Bee-one coils"). Here the reference to radiofrequencies is simply the fact that Larmor precession frequencies are typically in the radio frequency range of the electromagnetic spectrum. More often than not RF coils are "tuned"; inductive and capacitive elements in the circuit are balanced so that the net electrical impedance is purely resistive at the Larmor frequency. This facilitates efficient coupling between the transmitter and the coil, and hence efficient production of the largest possible B_1 field amplitudes.

Normally RF coils are designed to produce a reasonably homogeneous oscillating field over the volume to be

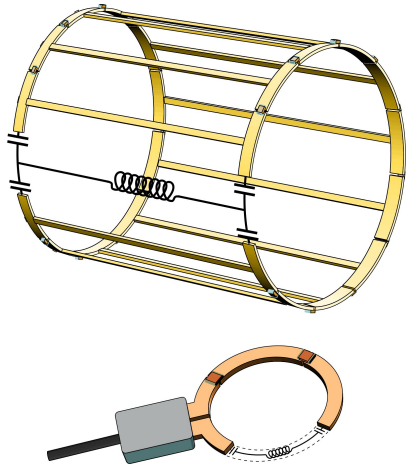


Figure 11: A surface coil (lower) and a birdcage coil (upper), both of which can function as a transmit (TX) coil, a receive (RX) coil, or a combined TX/RX coil. A few of the capacitive and inductive elements in each coil are shown schematically.

imaged, in order to generate reasonably uniform flip angles [60, 61]. Some designs involve little more than a circular conducting loop, tuned to resonate at the Larmor frequency. A current flowing through this loop produces a magnetic field that is roughly aligned with its axis, and that is reasonably strong out to a distance of order its radius. This is an example of a "surface coil" (see Fig. 11); it is convenient in situations where the tissues of interest are close to the surface, and flip angle homogeneity is not terribly important. Other RF coils involve more sophisticated arrangements of current paths. The birdcage coil, for example, involves a series of long straight parallel conductors uniformly arranged around the periphery of a cylinder (Fig. 11). These conductors act like inductors, and are carefully and individually tuned with capacitors to produce a resonance at the desired frequency; at resonance, the current flowing through the wires at any instant in time is a sinusoidal function of the azimuthal angle. This arrangement is an example of a "volume coil"; it produces a very homogeneous B_1 field directed perpendicular to the axis of the cylinder. Importantly, the intensity of this field remains constant in time while its direction rotates. In the reference frame rotating at the Larmor frequency this field is constant.

The use of coils like the birdcage that produce rotating or "circularly polarized" B_1 fields (as opposed to linearly polarized fields, cf. Fig. 10) can be very important at high frequencies where essentially all of the energy delivered to the coil by the transmitter is ultimately dissipated in the subject. In effect, half of a linearly polarized oscillating field is wasted from an NMR perspective. It does, however, contribute to the rate at which energy is deposited in the subject. This point is discussed further in section 2.2.4.

2.2.2 Faraday's Law: NMR detection

A changing magnetic field creates an electric field. The faster the magnetic field changes, the more intense is the resulting electric field. This is the essence of Faraday's Law of Induction,[10] which forms the basis for the detection of most NMR signals.

The net precessing nuclear magnetization that is established after a tipping pulse is applied has associated with it a small magnetic field whose orientation rotates about the z-axis at the Larmor frequency. This changing magnetic field produces an associated electric field, which also changes as a function of time. If an open loop of wire (or a coil with many turns) is placed near the region in which the precessing nuclei are situated, and arranged so that it intercepts some of the changing magnetic flux produced by those nuclei, an *electromotive force* (emf) or potential difference will be established between its two ends (see Fig. 12). This emf is proportional to the amplitude of

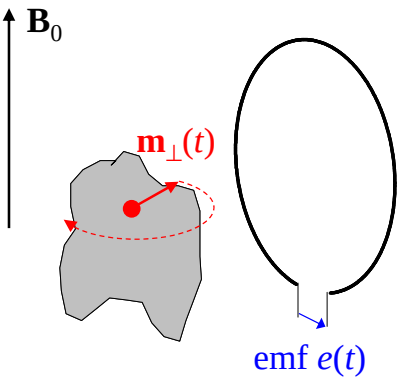


Figure 12: An elementary volume (the red sphere) within the magnetized sample (the grey volume) has a net magnetic moment $\mathbf{m}_\perp$. Its precession in the applied field $\mathbf{B}_0$ gives rise to an oscillating magnetic flux in the nearby detection loop, hence to an emf $e(t)$ oscillating at the corresponding Larmor frequency ω_0.

the transverse component of the precessing magnetization and to the precession frequency. It depends on the actual distribution of magnetization in an extended sample and on the geometry of the coil and sample. The principle of reciprocity [62] enables one to conveniently compute this elementary emf as a function of the coil shape and source position. The total emf, $e(t)$, induced around the loop is obtained by integration over the entire sample volume, taking into account variations in the phase of the nuclear magnetization across the sample and geometrical weighing factors. Typically the detected emf is very small, and needs to be amplified as soon as possible to avoid unnecessary degradation of signal quality due to interference from external noise sources. The use of tuned detection coils conveniently provides a significant enhancement prior to

[10] As was the case with Ampère's Law in the previous section, Faraday's Law provides a precise mathematical connection between B and E.

amplification. For a tuned coil with quality factor Q, the resulting *signal* is $S(t) = Qe(t)$.

The coil used to detect nuclear precession signals is another RF coil, in the sense that it operates at the same frequency as the B_1 coil. It is typically referred to as a detection coil, receive coil (or antenna), RX coil, or a pick-up coil. In some cases the same physical coil is used for both transmit and receive functions, but more often than not one wants to minimize crosstalk or interference between the two. When two coils are used, efforts are made to ensure that they are orthogonal. If this isn't done, the intense B_1 field produced by the transmit coil will induce an enormous emf across the terminals of the receive coil, complicating attempts to detect subsequent nuclear induction signals.

Just as is the case for B_1 coils, one is often interested in using volume detection coils designed to have reasonably uniform sensitivity to precessing magnetization over the entire volume of interest. In such cases, signals are approximately proportional to the total (integrated) magnetization of the sample. Alternatively, surface coils, or arrays of surface coils can be employed. The recorded signal(s) from these arrays provide coarse information about the location of the magnetization within the sample [38, 39].

2.2.3 Signal amplitude considerations

It is often stated that NMR is an inherently insensitive experimental probe. What is meant by this is that the conventional signature of NMR precession – the induced emf $e\,(t)$ discussed in the preceding section – is invariably a weak signal that is readily obscured by noise. Weak or not, those signals still encode a wealth of information about the local magnetic environment in which the sample nuclei are immersed.

Qualitative appreciation for the relative strength or weakness of conventional NMR signals can be gleaned through considering alternative methods for monitoring nuclear precession that were developed early in the history of the field. Rabi's 1938 demonstration of NMR [19], for example, involved measuring the flux of molecules in a weak but fully polarized beam. A deflection of the beam, and hence a change in detected intensity, was observed when an oscillating magnetic field was applied at the Larmor frequency. Two decades later Brossel and Cagnac [63] realized Kastler's proposal [64] for optical detection of nuclear magnetic resonance in optically polarized atomic vapours. A change in the polarization of fluorescent light emitted by low density Hg vapour was observed in response to a change in the nuclear spin state, driven by an oscillating magnetic field applied at the Larmor frequency. These pioneering experiments have two features in common that distinguish them from conventional NMR. First, in both cases the measurement was indirect, involving the detection of molecules or visible photons rather than the magnetic field produced by nuclei. The energy scale associated with each detected event (molecule or photon) was in the electron-Volt range: 9 orders of magnitude more than the energy difference between the two nuclear spin states in the applied magnetic field (see Table 1 for characteristic values). Second, in both cases the nuclear polarization was very far from equilibrium ($|p_{\rm up} - p_{\rm down}| \approx 1$), dramatically enhancing the contrast between measurements performed on- and off-resonance. Recall here for scale that the equilibrium nuclear polarization at room temperature in a 1 Tesla magnetic field is of order 10^{-6} or 1 ppm, and yet smaller in weaker fields. Combined, these features represent an astounding 15 order-of-magnitude advantage (or enhancement in signal amplitude) relative to direct detection of the nuclear transition under equivalent conditions. Of course this discrepancy is compensated in part through the huge increase in density that is obtained when liquid or solid samples are employed rather than molecular beams of dilute atomic vapours. Nevertheless, one is left with the naïve impression that direct detection of NMR presents a daunting signal acquisition problem relative to the highly leveraged schemes described above.

A proper evaluation of this problem requires consideration of two parameters: the amplitude of the detected signal and the amplitude of the detected noise. The quality of the signal is then expressed in terms of a signal-to-noise ratio (SNR). For given sample and coil geometries the detected emf $e\,(t)$ in conventional NMR scales as B_0^2; one factor of B_0 comes from the dependence of the equilibrium magnetization on field (cf. Eq. 1) and the other comes from the fact that the induced emf is proportional to the time derivative of the precessing magnetization (Faraday's law) and hence $\omega_0 = |\gamma B_0|$ (cf. Eq. 3). Estimating the field dependence of the detected noise is more involved, and requires an understanding of its physical origin. Here it is useful to make a distinction between extrinsic and intrinsic sources. Noise from extrinsic sources, such as RF interference (often referred to as electromagnetic interference or EMI) or noise generated by amplifiers and recording electronics can typically be suppressed or minimized through design: MRI systems are typically installed in a shielded room (or Faraday cage) for precisely this reason. Noise from intrinsic sources, on the other hand, is unavoidable: it typically arises from thermal agitation of electrical charges (Johnson noise) in the sample and the detection coil. If the sample is the dominant source of intrinsic noise, Faraday's law introduces the same factor of $\omega_0 = |\gamma B_0|$ to the corresponding induced emf as it does for the signal, and so the SNR increases linearly with B_0. If the coil is the dominant source of intrinsic noise, on the other hand, SNR increases more rapidly as the operating field is increased, scaling as $B_0^{7/4}$ [65, 66].

For most clinical imaging applications, the sample (i.e. tissues in the subject's body) acts as the dominant source of intrinsic noise, particularly as the operating field is increased. Conversely, in low or very-low magnetic fields, when small samples are employed (as is the case for MRI of small animals or in MR microscopy experiments) or

when non-conducting samples are probed, the detection coil tends to dominate the intrinsic noise. In such cases it can be advantageous to use cold probes or even superconducting coils [67]. The spectral density of thermal noise appearing across a resistor R at temperature T is given by $\sqrt{4k_B RT}$, and so gains are realized through reducing both R and T. More exotic options for enhancing SNR in MRI for niche applications are being explored, such as the use of SQUID-based detectors [68] and optical magnetometers [69] for ultra-low field applications and force-detection in magnetic resonance force microscopy for sub-micron resolution MRI [70].

2.2.4 Health safety considerations

The application of time-varying magnetic fields can lead to undesirable effects. Intense RF tipping pulses induce strong Faraday electric fields, which can in turn drive eddy currents and cause energy dissipation in the tissues of a subject. This energy dissipation rate has a strong frequency dependence, scaling as ω^2 over many decades in frequency [66]. In high field MRI systems, where RF frequencies in the VHF band of the electromagnetic spectrum (30-300 MHz) and above are employed, situations can arise in which most of the RF power delivered to the B_1 coil is dissipated in the subject [71, 72]. Likewise, fast switching of magnetic field gradients can also induce strong Faraday electric fields. In this case the characteristic frequencies are much lower and energy dissipation in the subject is usually not a concern. Instead, the induced electric fields E can cause peripheral nerve stimulation [73]. In both cases, restrictions and standards imposed by regulatory bodies and international commissions [73] limit the maximum permissible Faraday electric fields that can be induced. For RF fields, these limitations are normally expressed in term of specific absorption rates (SARs); for switched magnetic field gradients limitations are variously expressed in terms of peak values of dB/dt and/or E, as well as direct volunteer-based observations of nerve stimulation thresholds.

3 Fundamentals of MRI

This chapter began with a brief and qualitative description of Paul Lauterbur's first published MR imaging experiment, as summarized in Fig. 1. In this section we revisit that experiment, and examine somewhat more precisely the nature of the 1-D projections of the "NMR response" that he obtained. We then survey a few key modern approaches to MR image acquisition, based on the use of pulsed NMR and Fourier transform methods. In effect, this sets the stage for the remainder of the book.

This section is organized into three parts. The first deals with methods for generating 1-D projection images. The second deals with the acquisition of data for 2-D and 3-D images, and the third identifies the primary methods through which the "NMR response" is tuned or adapted to reflect different aspects of the nuclear environment. It is at this point in the process — the sensitization of NMR signals to different "contrast mechanisms" — that crucial connections are formed between acquired data and the underlying structure and function of the tissues that are imaged.

3.1 Effect of a field gradient: 1-D imaging

Consider a uniform magnetic field $\mathbf{B}_0 = B_0\hat{z}$ upon which is superimposed a uniform gradient $G \equiv dB_z/dk$, in the direction $\hat{k}$. The strength of the resulting magnetic field is a function of position $\mathbf{r}$. As long as concomitant gradients can be ignored, it can be written:

$$B_0(\mathbf{r}) = B_0(0) + G\hat{\mathbf{k}} \cdot \mathbf{r} \ . \tag{16}$$

The Larmor precession frequency of nuclei subjected to this field similarly becomes a linear function of position, and takes on the same value in any given plane oriented perpendicular to $\hat{k}$. If a time-varying magnetic field $\mathbf{B}_1$ oriented perpendicular to $\hat{z}$ is then applied at angular frequency ω, resonance will only occur in the vicinity of one such plane. For a CW NMR experiment, where the field B_1 is applied continuously (CW $\equiv$ continuous wave), the width of this region is of order $\delta r = 1/(\gamma G T_2)$.

If the NMR signal is received using a coil that has uniform coupling to all parts of the sample (e.g. a long solenoid, or a birdcage coil), its amplitude is proportional to the number of nuclei in the band that is excited. Sweeping or stepping the frequency ω or the field B_0 causes the resonant band to translate across the sample, generating a 1-D map or projection image of the magnetization density. The frequency (or field) scale for this mapping is set by the strength G of the field gradient. More precisely, the projection represents the convolution of a Lorentzian line shape (whose width is set by the spin-spin relaxation rate $1/T_2$) with the net nuclear magnetization density. As long as $1/T_2$ is appropriately small, the signal reflects the spatial distribution of M_0. This is illustrated in Fig. 13a, which shows the spectrum that is expected for a magnetic field gradient applied perpendicular to the axis of a cylindrical sample of radius a. It thus represents the signal that Lauterbur would have observed had he used only one tube in his experiments. By using two tubes instead of one, and by varying the direction $\hat{k}$ in which the gradient was applied relative to their axes, he was able to resolve both their physical extent and their apparent separation, as illustrated in Fig. 13b. In the remainder of this section we will assume that $1/(\gamma G a T_2) \ll 1$ and that the effects of diffusion can be ignored.

The procedure outlined above – sweeping the static magnetic field (or the frequency at which the field B_1 is applied) and collecting CW NMR spectra for various field gradient orientations – is time consuming. Most modern implementations of Lauterbur's experiment employ pulsed NMR, during which the field B_1 is only applied for finite periods of time. Subsequent to these tipping pulses, the

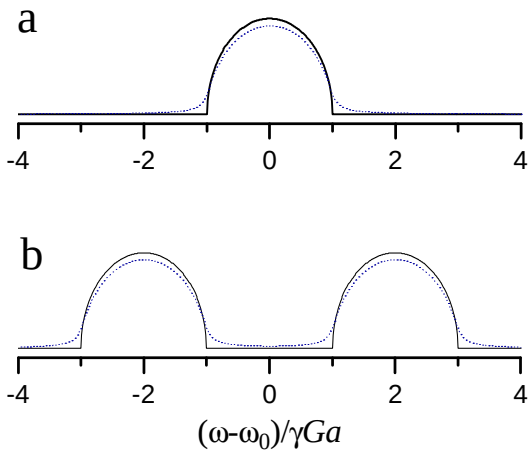


Figure 13: (a) Anticipated CW NMR spectra for a cylindrical sample of radius a in a uniform magnetic field gradient G applied perpendicular to its axis. Solid line: Ignoring the effects of relaxation, the spectrum is proportional to $\sqrt{1-(\omega-\omega_0)^2/(\gamma G a)^2}$, which is simply the projected width of the cylinder at a distance $(\omega-\omega_0)/(\gamma G a)$ from its axis. Dotted line: With some relaxation added to the Bloch equations (but ignoring the effects of diffusion), sharp features are smoothed out; here $\gamma G a T_2 = 2$. (b) Anticipated spectra for two parallel cylindrical samples, a situation modelling Lauterbur's experiment summarized in Fig. 1. Solid and dotted lines correspond to relaxation being ignored or included, as in (a).

nuclear magnetization $\mathbf{M}$ undergoes free precession and induces a time-varying emf in the detection coil:

$$e(t) \propto \int_{\text{sample}} M_\perp^0(\mathbf{r}) \cos\left[\gamma B_0(\mathbf{r}) t + \varphi\right] e^{-t/T_2} \ . \qquad (17)$$

Here $M_\perp^0(\mathbf{r})$ is the local amplitude of the transverse magnetization immediately after the tipping pulse (at time $t = 0$), the local position-dependent Larmor frequency $\gamma B_0(\mathbf{r})$ depends on the local magnetic field strength (given by Eq. 16) and the phase φ is a parameter that depends on the particular tipping pulse that is applied and on the position of the coil with respect to the sample.

Normally, the signal that is actually recorded during a pulsed NMR experiment is obtained by mixing the detected high-frequency emf $e(t)$ with a reference signal at a comparable frequency and fixed phase. The reference signal is often referred to as the local oscillator or "LO," and also forms the basis for generating the field B_1. A common choice is thus to set $\omega_{\text{LO}} = \gamma B_0(0)$. The resulting "signal"[11]

$$S(t) = \int_{\text{sample}} M_\perp^0(\mathbf{r}) \exp\left[i\left(\gamma G \hat{k}\cdot\mathbf{r}\right) t\right] e^{-t/T_2} \qquad (18)$$

is complex. It has two components; one that is in-phase with the LO and another that is 90° out-of-phase (or "in-quadrature") with the LO. These are are referred to as the real and imaginary parts of the signal, respectively. Equation 18 represents the sum of contributions to the detected emf arriving from all parts of the sample, as viewed in a frame of reference rotating at the local oscillator frequency ω_{LO}. The complex nature of $S(t)$ keeps track of the sense of rotation in the rotating frame, and thus discriminates between frequencies that are above or below ω_{LO}.

[11] $S(t)$ is only called the signal for convenience. It is merely proportional to the voltages that are digitized and recorded.

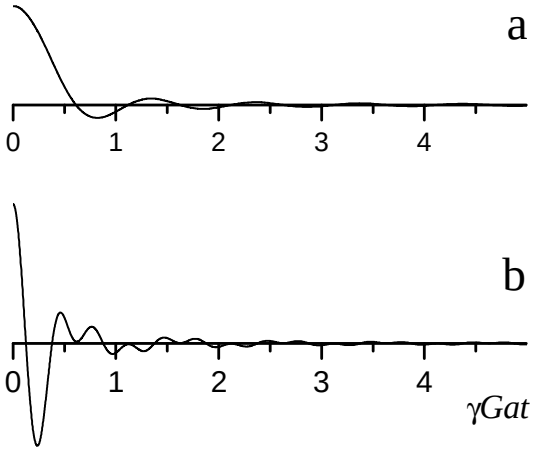


Figure 14: (a) Real part of the NMR free induction decay signal (Eq. 18) anticipated for a cylindrical sample of radius a in a uniform magnetic field gradient of amplitude G directed perpendicular to its axis, as was the case in Fig. 13a. The phase of the signal is constant, and its imaginary or quadrature component (not displayed) is zero at all times. The effects of relaxation and diffusion have been ignored. (b) Anticipated signal for two parallel cylinders, analogous to the situation in Fig. 13b.

Figure 14a shows the anticipated signal $S(t)$ following a single tipping pulse applied to the same cylindrical sample used to generate Fig. 13a. The rapid apparent attenuation of this "free induction decay" or FID merely reflects the fact that a magnetic field gradient has been imposed. The nuclear precession frequency varies as a function of position across the sample or subject, and the net emf detected by the coil is subject to destructive interference between the contributions generated at different locations (cf. Fig. 12). For a sample of size a the characteristic timescale for the apparent decay of $S(t)$ is of order $1/(\gamma G a)$. Figure 14b shows the expected signal for the sample of Fig. 13b: the high frequency modulation within the same overall signal lifetime corresponds to interference, or "beats," between contributions from the two tubes. This illustrates how an applied frequency encoding gradient links spatial characteristics of a sample to spectral features in the acquired data.

The information present in Fig. 14 can be used to recover the same spectra as were obtained in the CW NMR experiment. All that is required is a calculation of the Fourier transform of $S(t)$ after setting

$S(-t)=S^*(t)$, where the $*$ indicates complex conjugation. This Fourier transform represents the distribution of frequencies present in the FID, and hence the distribution of nuclear precession frequencies in the sample as the FID was recorded. Thus, apart from the necessary computations, the time required to obtain a 1-D projection image of the sample via pulsed NMR is dramatically reduced relative to the CW approach outlined earlier.

The dephasing of the precessing magnetization that is responsible for the apparent decay in Fig. 14 occurs on a timescale that is short compared to that set by relaxation (i.e. T_2). It can be represented pictorially with a series of isochromats, as was done in Fig. 6. Similarly, it can be refocussed in order to generate spin- or gradient-echoes. So, for example, if the direction of the field gradient is inverted at time τ, the recorded signal at subsequent times (i.e. $t > \tau$) becomes

$$S(t) = \int_{\text{sample}} M_\perp^0(\mathbf{r}) \exp\left[i\left(\gamma G\hat{k}\cdot\mathbf{r}\right)(2\tau - t)\right] e^{-t/T_2} \ . \quad (19)$$

Spins that were initially precessing faster than average end up precessing slower after the inversion, and vice versa. By the time $t = 2\tau$ the net phase accumulated by all spins in the sample is the same and an echo is formed. The amplitude of the recorded signal at $t = 2\tau$ is the same as it was at $t = 0$, to the extent that relaxation and diffusion can be ignored. Moreover, the recorded signal at times $t > 2\tau$ evolves just as it did immediately after the tipping pulse (cf. Fig. 14). And, just as was the case for the initial FID, calculating the Fourier transform of the recorded echo data yields a 1-D projection image of the sample.

This gradient echo formation procedure can be generalized. For example, the sense in which G is applied can be periodically reversed at times τ, 3τ, 5τ, ... as shown in Fig. 15a to form an echo train; that is, a periodic revival of phase coherence across the sample. The inevitable decay of the peak response every time an echo is formed provides information about irreversible processes like relaxation and diffusion. More generally, the strength of the field gradient before and after the reversal can be changed; an echo is then formed every time the time integral of $G(t)$ vanishes.

Alternatively, the spin-echo procedure outlined in connection with Fig. 6 can be used to generate echoes and echo trains as shown in Fig. 15b. In this case the gradient G remains the same but the phase of the magnetization is inverted by applying 180° tipping pulses about any axis in the transverse plane. The phase advance of "fast" spins near one end of the sample suddenly becomes a phase lag, and vice versa for "slow" spins at the other end. If the inversion occurs at time τ, an echo is formed at time 2τ.

Hard or soft pulses: which spins are excited?

When a magnetic field gradient G is present, the spatial uniformity of the flip angle induced by an RF pulse depends critically on the amplitude of the field B_1. This effect was alluded to in connection with Fig. 5. When an intense RF pulse is applied, the effective magnetic field $\mathbf{B}_{\text{eff}}$ in the rotating frame is dominated by $\mathbf{B}_1$. The angle ψ shown in Fig. 5 is thus always very close to 90° and the trajectory traced by the tip of the magnetization vector $\mathbf{M}$ on the Bloch sphere is essentially part of a great circle. The condition required for this to be true everywhere in the sample is that $B_1 \gg Ga$, where a is the size or extent of the object in the direction that G is applied. This condition defines what is known as a "hard pulse." The free induction decay pictured in Fig. 14 was implicitly launched using a hard RF pulse; even though a magnetic field gradient was present, the trajectory of $\mathbf{M}$ during the pulse, and the initial phase of the transverse magnetization immediately afterward, were effectively the same at all points in the sample.
A very different result is obtained when a "soft pulse" is applied. In this limit $B_1 \ll Ga$, and the effective magnetic field $\mathbf{B}_{\text{eff}}$ in the rotating frame is dominated by the apparent field $\mathbf{B}_{\text{app}}$ (Eq. 5), which – because of the applied gradient – is a function of position. To first approximation only spins located near the plane $\hat{k}\cdot\mathbf{r} = (\omega - \omega_0)/(\gamma G)$ are strongly influenced by B_1. This forms the basis for "slice selection," which is discussed further in section 3.2. The width of the region over which a soft pulse is effective in rotating the magnetization depends on the duration of the pulse, and the spatial profile of the flip angle can be controlled by the shape of the RF pulse envelope in time.

The signals that are obtained when spin- and gradient-echoes are formed are similar, but they are not identical. Experimental constraints often dictate the selection of one approach over the other. For example, a weakness of the gradient-echo technique is that the inversion of field gradients is usually imperfect. The current delivered to the gradient coils (and hence the field they produce) can certainly be inverted, but the static magnetic field itself is never perfectly unform. Thus, inverting the applied magnetic field gradient G is not quite the same as inverting the total magnetic field gradient. Even worse, when strong gradients are applied (or weak magnetic fields are employed), the notion of a magnetic field gradient itself breaks down, and the influence of orthogonal components of the field on the time evolution of $\mathbf{M}$ needs to be considered. In either case, a progressive loss of phase coherence occurs on a timescale that is often shorter than the transverse relaxation time T_2. This particular limitation can be eliminated by generating spin-echoes instead of gradi-

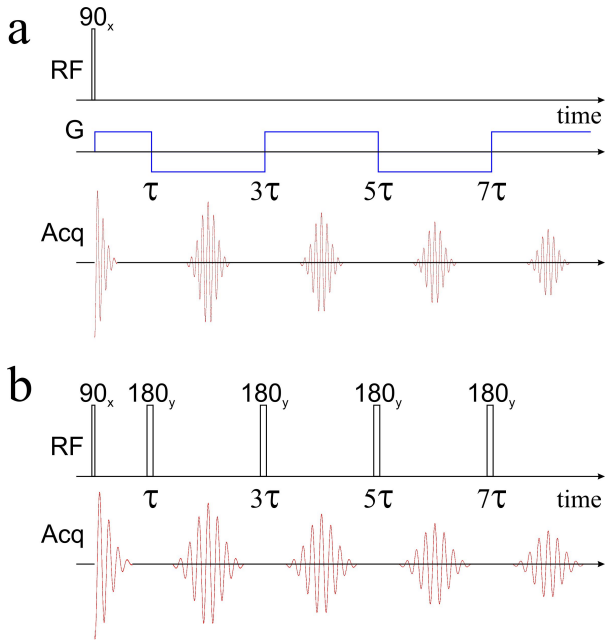


Figure 15: Schematic diagram showing the synchronization of applied B_1 fields (RF), switched gradient fields (G), and acquired nuclear induction signals (Acq) for two pulse sequences. Both begin with a 90° RF tipping pulse that rotates the thermal equilibrium magnetization into the transverse plane. In the first example (panel a) the sense of the applied magnetic field gradient G is periodically reversed, creating a train of gradient echoes In the second example (panel b) the phase of the magnetization is periodically inverted by applying 180° tipping pulses, creating a train of spin echoes. The time between the initial RF pulse and the peak of the first echo (or the time between successive echoes) is referred to as the echo time and is conventionally denoted TE or T_{E} Often, sequences such as those shown here are repeated, in which case the repetition time (the time between successive applications of the sequence) is conventionally denoted TR or T_{R}.

ent echoes. To the extent that perfect and uniform 180° tipping pulses can be generated, inverting the phase of the magnetization leads to coherent echo formation irrespective of imperfections in B_0. On the other hand, a limiting factor for spin-echo sequences when human subjects are involved is the need to employ short, high amplitude B_1 fields in order to obtain uniform 180° rotations. In high field systems the energy associated with these pulses is invariably deposited in the subject, and can pose a safety hazard (cf. section 2.2.4).

Ultimately, the precision of the spectrum representing the 1-D distribution of the precessing magnetization that is obtained from the Fourier transform of the recorded signal is limited. The time variation of $S(t)$ is sampled at discrete points in time (at a sampling frequency f_{s}), and over a finite period of time (T_{obs}) that is usually centred[12] on the echo formation time 2τ or $2n\tau$. The spectrum obtained from these data (through a discrete Fourier transform procedure) has a frequency resolution $1/T_{\mathrm{obs}}$ and extends over a frequency range $\pm f_{\mathrm{s}}/2$. This frequency resolution limits the maximum spatial resolution of the 1-D projection image described above to $1/(\gamma G T_{\mathrm{obs}})$. Factors such as a finite transverse relaxation time T_2 (cf. Fig. 13), diffusion, and noise (cf. section 2.2.3) all serve to reduce this maximum resolution. The frequency range also plays an important role; it imposes a finite field-of-view (FOV) given by $f_{\mathrm{s}}/(\gamma G)$. The FOV must be larger than the physical extent of the sample or subject; otherwise folding artifacts associated with under-sampling of high frequency components of the signal can occur.

3.2 2-D and 3-D imaging methods

Paul Lauterbur's 2-D NMR images of water-filled capillaries (such as the one shown in Fig. 1) were obtained through a process of mathematical inference known as "back projection." This involves combining several 1-D or "line" images, each acquired in a different direction in the same plane, to form a 2-D image on a grid of points by iteratively modelling the unknown distribution of nuclear magnetization. While this approach to image reconstruction played an important role in the early evolution of MRI, it is not often used today. Modern MR image reconstruction relies heavily on the phase- and frequency-encoding of the (precessing) nuclear magnetization in a sample, multi-dimensional Fourier transform techniques, and the selective excitation of nuclei in specific, well-defined planes or bands intersecting the sample or subject. The general principles by which MR image data is acquired are discussed below. We begin with the process of "slice selection," which is ubiquitous in modern MRI.

A soft RF tipping pulse applied in the presence of a magnetic field gradient $G\hat{k}$ is selective. Maximum rotation of the magnetization vector is obtained in the plane defined by $\hat{k} \cdot \mathbf{r} = (\omega - \omega_0)/(\gamma G)$; elsewhere the effect is much smaller. For small tip angles[13] the spatial width of the region that is influenced is proportional to the spectral width of the pulse, which is in turn inversely proportional to its duration in time τ. Rectangular RF pulse envelopes, where the field B_1 has a constant amplitude for a finite period of time, yield awkward sinc-shaped slice profiles in

[12] The observation window does not have to be centred on the echo time; a recording of half of the echo, starting or ending with the signal at the echo time is sufficient. This is possible because of the symmetry of echoes, which result from the fact that the phase of the precessing magnetization was uniform at the start of the experiment. A full recording of a FID starting immediately after a tipping pulse (as implied by the example shown in Fig. 14) is often technically difficult to acquire; a delay following the tipping pulse is normally required to avoid saturation of the detection electronics by the applied B_1 field. A symmetric echo is usually recorded to increase SNR, but asymmetric echoes are often used in ultra-fast acquisition schemes.

[13] More sophisticated pulse shaping procedures are required when large tip angles are desired [74], because of the non-linear dependence of flip angle on RF amplitude and detuning illustrated in Fig. 5.

space; the plane on which the maximum rotation is obtained is symmetrically flanked by a series of side lobes. A sinc-shaped RF pulse envelope is much more useful. Modulating the amplitude of B_1 in time such that

$$B_1(t) = B_1(0)\frac{\sin(\gamma G\,\Delta z\;t/2)}{\gamma G\,\Delta z\;t/2} \equiv \mathrm{sinc}\left(\frac{\gamma G\,\Delta z\;t}{2}\right) \quad (20)$$

yields a rectangular (uniform) slice of width Δz in space. Starting from thermal equilibrium, a soft sinc-shaped, small tip angle RF pulse applied in the presence of a "slice selection gradient" conveniently produces a transverse magnetization that is uniform in amplitude over this slice and zero elsewhere. This would be ideal for imaging if not for the fact that, by the end of the pulse, the magnetization is strongly dephased by the gradient. The simplest and most convenient way to deal with this is by generating a gradient-recalled echo. Rather than turning off the slice-selection gradient at the end of the RF pulse, its direction is momentarily reversed as shown in Fig. 16. At the point in time where the echo is formed ($t = T_e$), the transverse magnetization in the sample or subject is uniform in a well-defined slice of thickness Δz and zero elsewhere. This slice can be positioned anywhere in the sample by choosing an appropriate frequency for B_1. As long as a 2-D image can be generated from the selectively-excited magnetization in each slice, a full 3-D image can be recorded.

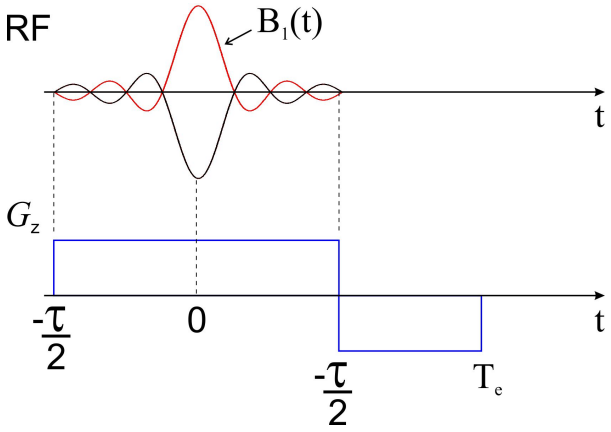


Figure 16: A soft sinc-shaped RF pulse for selective excitation of the transverse magnetization in a well-defined slice. The slice selection gradient G_z is reversed at the end of the RF pulse in order to unwind the accumulated phase of the magnetization. An echo is formed at the same instant that the gradient is turned off ($t = T_e$). The schematic depiction of the RF pulse only indicates the envelope or amplitude of $B_1(t)$ (cf. Eq. 20). The high frequency oscillation of B_1 at $\omega \sim \omega_0$ is not shown. Note that truncation of the sinc function distorts the rectangular slice profile. We have ignored such effects in this discussion.

A strategy for generating a 2-D image following slice selection is summarized in Fig. 17. It proceeds as follows. A gradient $\mathbf{G}_e$ is first applied in the plane of the slice for a time period τ_e. This establishes a gradient in the phase of the transverse magnetization as it undergoes free precession. This gradient is consequently referred to as a phase-encoding gradient. Next, a 180° RF pulse is applied at time $t = \tau > \tau_e$ to invert the phase of the precessing magnetization (relative to the phase of the pulse). A second gradient $\mathbf{G}_r$ is then applied in the plane of the slice but perpendicular to $\mathbf{G}_e$, in anticipation of the spin-echo generated by the 180° rotation. This gradient is known as a read gradient[14] because it is applied during signal acquisition.

As a concrete example, assume that a rectangular slice of thickness Δz has been selected perpendicular to the z axis and that $\mathbf{G}_r$ and $\mathbf{G}_e$ happen to be applied along the x- and y-axes, respectively. The recorded signal (analogous to Eq. 19) in the vicinity of the echo is of the form

$$S(t > \tau) = \int_{\text{sample}} M_\perp^0(\mathbf{r}) \exp\left[i\left(k_x(t)x + k_y y\right)\right] e^{-t/T_2} \quad (21)$$

where $k_x(t) = \gamma\,(2\tau - t)\,G_r$ and $k_y = \gamma\tau_e G_e$ are interpreted as components of a wave vector, describing the spatial modulation of the magnetization in the sample. Equivalently, the recorded signal represents

$$\begin{aligned} S(k_x, k_y) &= \int_{\text{sample}} M_\perp^0(\mathbf{r}) \exp\left[i\left(k_x x + k_y y\right)\right] e^{-t/T_2} \quad (22)\\ &= \Delta z \int_{\text{slice}} M_\perp^0(x,y) \exp\left[i\left(k_x x + k_y y\right)\right] e^{-t/T_2} \end{aligned}$$

at a fixed value of k_y and over a range of k_x. More generally, ignoring attenuation and assuming $S(k_x, k_y)$ is known for all values of k_x and k_y, the two-dimensional inverse Fourier transform of Eq. 22 is $M_\perp^0(x,y)\Delta z \propto M_\perp^0(x,y)$, which is the desired two-dimensional spatial distribution of nuclear magnetization in the slice.

In practice, the sequence shown in Fig. 17 is repeated N_e times for evenly spaced values of k_y corresponding to phase-encoding gradients in the range $-G_{\max} < G_e < G_{\max}$. Each iteration probes $S(k_x, k_y)$ for evenly spaced values of k_x set by the sampling rate f_s and the acquisition time. The result is a 2-D Cartesian array of data spanning a range of "k-space," as shown in Fig. 18a. The (discrete) 2-D inverse Fourier transform of this data corresponds to a 2-D image of the transverse nuclear magnetization in the slice. The FOVs in the direction of the read-gradient and the direction of the phase-encoding gradient are $f_s/(\gamma G_r)$ and $N_e/(2\gamma\tau_e G_{\max})$, respectively.

[14] It is also referred to as a frequency encoding gradient, in connection to the manner in which it is employed for Fourier transform spectroscopy. For imaging, signals are processed in terms of the spatial modulation of the magnetization in the sample (k-space) rather than frequency.

k-space in MRI

The signals that are detected and recorded in MRI do not usually come from localized regions of the sample or subject. Rather, they represent spatially-modulated depictions of the nuclear magnetization integrated over the entire volume to which the receive coils are sensitive. This spatial modulation is imposed and controlled by the linear magnetic field gradients that are applied, and can be characterized by a wave vector $\mathbf{k}$. A mathematical analysis of this problem shows that the detected signals are nothing more than Fourier transforms (or a spatial frequency representation) of the nuclear magnetization distribution that is being imaged.

The space in which the coordinates k_x and k_y of the wave vector $\mathbf{k}$ are the natural parameters of the recorded signal $S(k_x, k_y)$ is conventionally referred to as *k-space* or *reciprocal space*. As long as enough data are acquired to characterize $S(k_x, k_y)$ in reciprocal space, one need only perform an inverse Fourier transform to reconstruct an image of the magnetization distribution in real space [75, 76, 77, 78].

Imaging sequences, such as the one shown in Fig. 18, are often thought of as being recipes or instructions for acquiring data that span k-space. Strictly speaking, standard receive coils only sense the average nuclear magnetization and hence only monitor the centre of k-space. It is actually the Fourier transform of the magnetization that traverses k-space as the imaging sequence is executed. Nevertheless, all of the information needed for image reconstruction is still acquired.

The concept of k-space or reciprocal space is commonplace in disciplines such as crystallography, solid-state physics, and optics. Often one is able to view or resolve key features of a complex system much more clearly in k-space than in real space. An important example is the phenomenon of Bragg diffraction, which occurs when coherent short-wavelength radiation is scattered from the lattice planes of a crystalline solid or other periodic structure. This is not the case in MRI. Generally, little or no useful information is evident when one looks at raw k-space MRI data. It is only when the real space image is reconstructed that useful information is revealed.

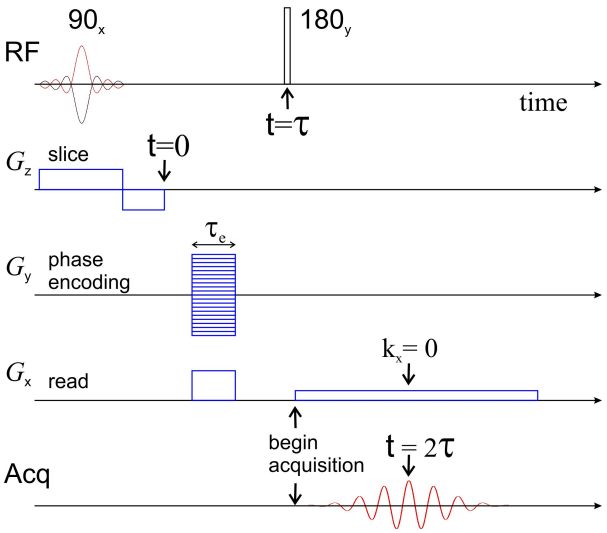


Figure 17: Outline of a sequence for two-dimensional Fourier transform imaging. The first RF pulse in the presence of a gradient ($G_z\hat{z}$) excites one rectangular slice of the sample (cf. Fig.16). The second RF pulse at $t = \tau$ generates a spin echo that peaks at time $t = 2\tau$. A phase-encoding gradient ($\mathbf{G}_e \equiv G_y\hat{y}$) applied during the first free evolution period establishes a gradient in the phase of the transverse magnetization along the y-axis. Each time this sequence is repeated, a different phase encoding gradient is employed. An orthogonal read (or frequency-encoding) gradient ($\mathbf{G}_r \equiv G_x\hat{x}$) is then applied while the echo is acquired. The read gradient causes the transverse magnetization to dephase, and so an extra gradient pulse is applied along $\hat{x}$ during the first free-evolution period to compensate. The net phase shift caused by the read gradient at the echo maximum is thus zero. In practice, refinements to this basic scheme (such as the use of a selective 180° RF pulse) are often either necessary or desirable.

Many variants of this basic strategy exist. For example, the spin-echoes generated by the sequence shown in Fig 17 are readily replaced with gradient-recalled echoes, which in some cases is useful for fast imaging. Even faster rates are possible when echo trains are formed after each excitation. In this way a different phase encoding gradient can be used each time the magnetization is refocussed, enabling rapid passage through k-space. This is the basic idea behind echo-planar imaging. Other approaches include radial acquisition schemes, as suggested in Fig. 18b. These enable frequent re-sampling of the centre of Fourier space, which can be used to help minimize movement artifacts to which other sequences are susceptible. It also permits fast time resolution using sliding window methods. Yet other strategies for acquiring data in k-space employ spiral (or interleaved spiral) trajectories or partial (e.g. half-plane) acquisition schemes [79].

3.3 Contrast

As described, the imaging strategies outlined in the previous section all have one thing in common: the acquired signal – and hence the image that is generated – nominally reflects the local magnetization density in the sample or subject. If proton NMR is employed, the signal strength scales with the density of H atoms, which are abundant in the water and lipids of all tissues. As a result, these strategies yield anatomical images with poor contrast and

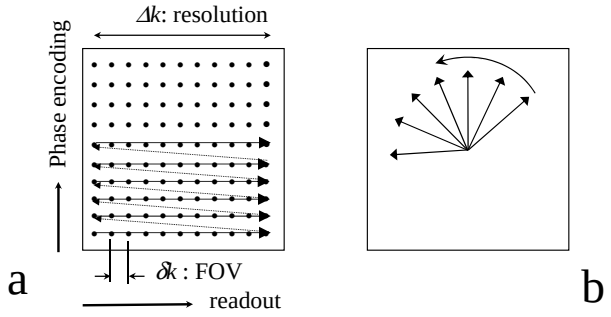


Figure 18: Examples of trajectories for 2-D k-space sampling. a: Cartesian mapping of the plane is obtained from a series of data acquisitions, each with different phase encoding in the Y direction. b: Radial mapping is obtained from acquisitions along different azimuthal directions, each one of which samples the centre of k-space.

are of little use from a clinical perspective. It is only when they are "tuned" or modified to probe physical processes that are tissue-specific that the real potential of MRI is realized. Sensitization – or "weighting" – of the acquired signal to these processes can yield significantly enhanced contrast between organs with similar proton density, or between regions characterized by normal and pathological behaviour. A brief summary of common image weighting schemes is given below.

Sensitization of acquired NMR signals to nuclear relaxation – irreversible processes characterized by the phenomenological parameters T_1 and T_2 – is the most obvious and most widely employed method of enhancing image contrast. In fact, Lauterbur's original demonstration of 2-D MR imaging included a T_1 sensitized image [1]. And, in connection with this image he noted that longer-than-normal values of T_1 had been observed in malignant tumours [80].

T_1-weighting of images is naturally obtained when the sequence repetition time T_R (or TR) is comparable to the longitudinal relaxation time. Endless repetition of the sequence under these conditions doesn't provide enough time for the magnetization to return to thermal equilibrium between iterations. As a result, the steady-state magnetization is suppressed relative to its thermal equilibrium value M_0 such that:

$$M = M_0 \frac{1 - \exp\left(-T_\mathrm{R}/T_1\right)}{1 - \cos\theta \exp\left(-T_\mathrm{R}/T_1\right)} \ , \qquad (23)$$

where θ is the tip angle of the RF pulse (cf. Fig. 4). For appropriate choices of θ and T_R, the magnetization in regions characterized by short values of T_1 will recover more than that in regions characterized by long values of T_1. They will thus provide larger amplitude signals and ultimately be rendered as more intense regions on an image. In normal tissues, fat (lipids) is characterized by shorter values of T_1 than water and thus it appears white in T_1-weighted MR images. Thus, cerebral white matter appears white on a T_1-weighted MR image because it contains more lipids than does grey matter.

T_2-weighting of images is obtained when the echo formation time T_e (or TE) is comparable to the transverse relaxation time T_2. Under these conditions, significant irreversible dephasing of the transverse magnetization occurs between the initial RF excitation (tipping pulse) and the measurement of the signal amplitude. This effect is responsible for the factor $\exp\left(-t/T_2\right)$ appearing in the various expressions for $S(t)$ and $S(k_x, k_y)$ in section 3.2; when $t = T_\mathrm{e} \sim T_2$, the resulting signal attenuation becomes significant. This is precisely the opposite of the effect observed for T_1-weighting. That is, regions characterized by strong T_2 relaxation yield relatively weak NMR signals and are rendered as being dark on a T_2-weighted image. Regions characterized by strong T_1 relaxation yield relatively strong NMR signals and are rendered as being bright on a T_1-weighted image. Lipid-rich regions tend to be characterized by stronger relaxation (both T_1 and T_2) than water-rich regions. They thus tend to appear relatively brighter in T_1-weighted images and darker in T_2-weighted images.

The intrinsic T_1- or T_2-weighted contrast induced by tissue structure or pathology is not always strong enough to reveal features or to enable a sensitive and specific diagnosis. In such cases it is sometimes possible to enhance contrast through the introduction of paramagnetic contrast agents. Gadolinium-based contrast media injected into the bloodstream, for example, enhance T_1 relaxation and yield a local increase in T_1-weighted signal intensity wherever blood perfusion is present. Small iron-oxide and other superparamagnetic particles, on the other hand, enhance T_2 relaxation and lead to a corresponding decrease in T_2-weighted signal intensity wherever they are present.

A third physical process that can be used for image contrast is diffusion, as was discussed in section 2.1.3. Like relaxation, diffusion naturally causes an irreversible degradation of NMR signal coherence. One method for diffusion-weighting MR images involves adding a bipolar field gradient pulse between the initial RF excitation and the rest of the normal sequence. The purpose of this bipolar gradient is to imprint a helix-like pattern on the phase of the magnetization along the direction of the diffusion-sensitizing gradient, and then unwind it. If the nuclear spins contributing to the NMR signal are stationary, this manipulation has no effect. But, if diffusion occurs on the timescale of the pulse, the net phase accumulated by a particular spin depends on the (random) path it happened to follow in the interim. The net result is an attenuation of the net transverse magnetization by a factor $\exp(-D\gamma^2 G^2 \tau_\mathrm{d}^3)$, where D is the relevant diffusion coefficient, G is the sensitizing gradient amplitude, and τ_d is a time scale associated with the duration of its application.[15] As with T_2-weighting, regions characterized by

[15] An alternate and commonly employed variant of this measurement involves the insertion of a time delay Δ between two short oppositely directed gradient pulses. In this case the degree to which

significant diffusion yield less signal than those characterized by little diffusion, and are thus rendered as being darker.

Diffusive motions are often *restricted*. Atoms or molecules might be relatively free to wander short distances ("free diffusion"), but then encounter barriers that impede longer range motion. In such cases, when pulsed-gradient NMR techniques are used to measure D, an *apparent diffusion coefficient* or ADC is observed. This ADC is invariably smaller than the free diffusion coefficient, but the factor by which it is reduced depends on the timescale over which the measurement is made. ADC imaging of the brain is routinely performed in case of ischemic or hemmoragic stroke.

An additional factor arises when the confining structures are anisotropic, as is the case with nerve fibre tracts. In this case ADC mapping can be performed as a function of the direction in which the sensitizing gradient is applied. The resulting diffusion-tensor images provide information about both the direction and magnitude of the underlying diffusion processes. Pulsed-field diffusion-tensor MR imaging of the brain enables visualization of white matter fibre tracts and can be used to map subtle changes associated with diseases such as multiple sclerosis or epilepsy.

The same general strategies used to characterize diffusion can be adapted to probe displacements and velocities (flow imaging), and have many applications to angiography.

References

[1] Lauterbur P (1973) Image formation by induced local interactions - examples employing nuclear magnetic-resonance. Nature 242:190–191

[2] Carr HY (1952) Free precession techniques in nuclear magnetic resonance. Ph.D. thesis, Harvard University

[3] Walters GK, Fairbank WM (1956) Phase separation in He3-He4 solutions. Phys. Rev. 103:262–263

[4] Osheroff DD, Gully WJ, Richardson RC, Lee DM (1972) New magnetic phenomena in liquid He^3 below 3 mK. Phys. Rev. Lett. 29:920

[5] Abragam A (1961) Principles of Nuclear Magnetism. Oxford Univeristy Press, Oxford

[6] Cowan B (1997) Nuclear Magnetic Resonance and Relaxation. Cambridge University Press, Cambridge

[7] Ernst RR, Bodenhausen G, Wokaun A (1987) Principles of Nuclear Magnetic Resonance in one and two dimensions. Oxford University Press, London/New York

[8] Slichter C (1990) Principles of Magnetic Resonance. Springer-Verlag, Berlin

[9] Levitt MH (2001) Spin Dynamics: Basics of Nuclear Magnetic Resonance. John Wiley & Sons, Ltd, West Sussex

[10] Callaghan PT (2011) Translational Dynamics and Magnetic Resonance: Principles of Pulsed Gradient Spin Echo NMR. Oxford University Press, Oxford

[11] Blümich B (2000) NMR Imaging of Materials. Clarendon Press, Oxford

[12] Brown MA, Semelka RC (2010) MRI: Basic Principles and Applications. John Wiley & Sons Inc., Hoboken, New Jersey

[13] Callaghan PT (1991) Principles of Nuclear Magnetic Resonance Microscopy. Oxford Univeristy Press, New York

[14] Kuperman V (2000) Magnetic Resonance Imaging: Physical Principles and Applications. Academic Press, New York

[15] Kimmich R (1997) NMR Tomography, Diffusometry, Relaxometry. Springer-Verlag, Berlin

[16] Purcell E, Torrey H, Pound R (1946) Resonance absorption by nuclear magnetic moments in a solid. Phys. Rev. 69:37–38

[17] Bloch F, Hansen W, Packard M (1946) Nuclear induction. Phys. Rev. 69:127

[18] Bloch F, Hansen W, Packard M (1946) The nuclear induction experiment. Phys. Rev. 70:474–485

[19] Rabi I, Zacharias J, Millman S, Kusch P (1938) A new method of measuring nuclear magnetic moment. Phys. Rev. 53:318

[20] Gerlach W, Stern O (1922) Das magnetische moment des silberatoms. Z. Physik 9:353

[21] Gorter C (1936) Negative result of an attempt to detect nuclear magnetic spins. Physica 3:995

[22] Gorter C, Broer L (1942) Negative result of an attempt to observe nuclear magnetic resonance in solids. Physica 9:591–596

[23] Torrey H (1949) Transient nutations in nuclear magnetic resonance. Phys. Rev. 76:1059–1068

[24] Hahn E (1950) Nuclear induction due to free Larmor precession. Phys. Rev. 77:297–299

[25] Bloch F (1946) Nuclear induction. Phys. Rev. 70:460–474

[26] Hahn EL (1950) Spin echoes. Phys. Rev. 80:580–594

the signal is attenuated by diffusion during this time period is characterized by a parameter that is conventionally referred to as the "b-value".

[27] Arnold JT, Dharmatti SS, Packard ME (1951) Chemical effects on nuclear induction signals from organic compounds. J. Chem. Phys. 19:507

[28] Singer J (1959) Blood flow rates by nuclear magnetic resonance measurement. Science 130:1652–1653

[29] Jackson J, Langham W (1968) Whole-body NMR spectrometer. Rev. Sci. Instrum. 39:510–&

[30] Garroway A, Grannell P, Mansfield P (1974) Image-formation in NMR by a selective irradiative process. J. Phys. C: Solid State Phys. 7:L457–L462

[31] Mansfield P, Maudsley A (1977) Planar spin imaging by NMR. J. Magn. Reson. 27:101–119

[32] Ernst R, Anderson W (1966) Application of Fourier transform spectroscopy to magnetic resonance. Rev. Sci. Instrum. 37:93

[33] Kumar A, Welti D, Ernst RR (1975) NMR fourier zeugmatography. J. Magn. Reson. 18:69–83

[34] Edelstein W, Hutchison J, Johnson G, Redpath T (1980) Spin warp NMR imaging and applications to human whole-body imaging. Phys. Med. Biol. 25:751–756

[35] OECD (2013). Magnetic resonance imaging units, total, Health: Key Tables from OECD, No. 36. doi: 10.1787/magresimaging-table-2013-2-en

[36] OECD (2013). Magnetic resonance imaging (MRI) exams, total, Health: Key Tables from OECD, No. 46. doi: 10.1787/mri-exam-total-table-2013-2-en

[37] Lustig M, Donoho D, Pauly JM (2007) Sparse MRI: The application of compressed sensing for rapid MR imaging. Magn. Reson. Med. 58:1182–1195

[38] Sodickson D, Manning W (1997) Simultaneous acquisition of spatial harmonics (SMASH): Fast imaging with radiofrequency coil arrays. Magn. Reson. Med. 38:591–603

[39] Pruessmann K, Weiger M, Scheidegger M, Boesiger P (1999) SENSE: Sensitivity encoding for fast MRI. Magn. Reson. Med. 42:952–962

[40] Kastler A (1950) Quelques suggestions concernant la production optique et la détection optique d'une inégalite de population des niveaux de quantification spatiale des atomes - Application à l'experience de Stern et Gerlach et à la résonance magnétique. J. Phys. Radium 11:255–265

[41] Colegrove FD, Schearer LD, Walters GK (1963) Polarization of He3 gas by optical pumping. Phys. Rev. 132:2561–2572

[42] Happer W (1972) Optical pumping. Rev. Mod. Phys. 44:169–249

[43] Abragam A, Goldman M (1978) Principles of dynamic nuclear polarisation. Rep. Prog. Phys. 41:395

[44] Natterer J, Bargon J (1997) Parahydrogen induced polarization. Prog. Nucl. Magn. Reson. Spectrosc. 31:293 – 315

[45] Ardenkjaer-Larsen J, Fridlund B, Gram A, Hansson G, et al. (2003) Increase in signal-to-noise ratio of $> 10,000$ times in liquid-state NMR. PNAS 100:10158–10163

[46] Mansson S, Johansson E, Magnusson P, Chai C, et al. (2006) C-13 imaging - a new diagnostic platform. Eur. Radiol. 16:57–67

[47] Ackerman JJH (2013) Magnetic resonance imaging: Silicon for the future. Nature Nanotechnology 8:313–315

[48] Cassidy MC, Chan HR, Ross BD, Bhattacharya PK, et al. (2013) In vivo magnetic resonance imaging of hyperpolarized silicon particles. Nature Nanotechnology 8:363–368

[49] Fogarty HA, Berthault P, Brotin T, Huber G, et al. (2007) A cryptophane core optimized for xenon encapsulation. J. Am. Chem. Soc. 129:10332+

[50] Klippel S, Doepfert J, Jayapaul J, Kunth M, et al. (2014) Cell Tracking with Caged Xenon: Using Cryptophanes as MRI Reporters upon Cellular Internalization. Angew. Chem. Int. Ed. 53:493–496

[51] Young I (2004) Significant events in the development of MRI. J. Magn. Reson. Imaging 20:183–186

[52] Jeener J (2000) Equivalence between the "classical" and the "Warren" approaches for the effects of long range dipolar couplings in liquid nuclear magnetic resonance. J. Chem. Phys. 112:5091–5094

[53] Hoult D, Ginsberg N (2001) The quantum origins of the free induction decay signal and spin noise. J. Magn. Reson. 148:182–199

[54] Hoult DI (2009) The Origins and Present Status of the Radio Wave Controversy in NMR. Concepts Mag. Reson. A 34A:193–216

[55] Bloembergen N, Purcell EM, Pound RV (1948) Relaxation effects in nuclear magnetic resonance absorption. Phys. Rev. 73:679–712

[56] Murali N, Krishnan V (2003) A primer for nuclear magnetic relaxation in liquids. Concepts Mag. Reson. A 17A:86–116

[57] Torrey HC (1956) Bloch equations with diffusion terms. Phys. Rev. 104:563–565

[58] Turner R (1993) Gradient coil design: A review of methods. Magnetic Resonance Imaging 11:903 – 920

[59] Hidalgo-Tobon S (2010) Theory of gradient coil design methods for magnetic resonance imaging. Concepts in Magnetic Resonance Part A 36A:223–242

[60] Mispelter J, Lupu M, Briguet A (2006) NMR Probeheads for Biophysical and Biomedical Experiments. Imperial College Press, London

[61] Vaughan JT, Griffiths JR (eds.) (2012) RF Coils for MRI. John Wiley & Sons

[62] Hoult DI (2000) The principle of reciprocity in signal strength calculationsa mathematical guide. Concepts in Magnetic Resonance 12:173–187

[63] Cagnac B, Brossel J, Kastler A (1958) Résonance magnétique nucléaire du mercure Hg-201 aligné par pompage optique. C.R. Acad. Sci. 246:1827–1830

[64] Kastler A (1957) Optical methods of atomic orientation and of magnetic resonance. J. Opt. Soc. Am. 47:460–465

[65] Hoult D, Lauterbur P (1979) Sensitivity of the zeugmatographic experiment involving human samples. J. Magn. Reson. 34:425–433

[66] Hayden ME, Bidinosti CP, Chapple EM (2012) Specific absorption rates and signal-to-noise ratio limitations for MRI in very-low magnetic fields. Concepts Mag. Reson. A 40A:281–294

[67] Bittoun J, Querleux B, Darrasse L (2006) Advances in MR imaging of the skin. NMR Biomed. 19:723–730

[68] Mossle M, Myers W, Lee S, Kelso N, et al. (2005) SQUID-detected in vivo MRI at microtesla magnetic fields. IEEE Transactions on Applied Superconductivity 15:757–760. 2004 Applied Superconductivity Conference, Jacksonville, FL, OCT 03-08, 2004

[69] Budker D, Romalis M (2007) Optical magnetometry. Nature Physics 3:227–234

[70] Mamin HJ, Poggio M, Degen CL, Rugar D (2007) Nuclear magnetic resonance imaging with 90-nm resolution. Nature Nanotechnology 2:301–306

[71] Homann H, Boernert P, Eggers H, Nehrke K, et al. (2011) Toward Individualized SAR Models and In Vivo Validation. Magn. Reson. Med. 66:1767–1776

[72] Wolf S, Diehl D, Gebhardt M, Mallow J, et al. (2013) SAR Simulations for High-Field MRI: How Much Detail, Effort, and Accuracy Is Needed? Magn. Reson. Med. 69:1157–1168

[73] International Electrotechnical Commission, Medical Electrical EquipmentPart 233: particular requirements for the basic safety and essential performance of magnetic resonance equipment for medical diagnosis. (2010)

[74] Pauly J, Leroux P, Nishimura D, Macovski A (1991) Parameter relations for the Shinnar-Leroux selective excitation pulse design algorithm. IEEE Transactions on Medical Imaging 10:53–65

[75] Ljunggren S (1983) A Simple Graphical Representation of Fourier-based Imaging Methods. J. Magn. Reson. 54:338–343

[76] Xiang Q, Henkelman R (1993) K-Space Description for MR Imaging of Dynamic Objects. Magn. Reson. Med. 29:422–428

[77] Hennig J (1999) K-space sampling strategies. Eur. Radiol. 9:1020–1031

[78] Paschal C, Morris H (2004) k-space in the clinic. J. Magn. Reson. Imaging 19:145–159

[79] McGibney G, Smith M, Nichols S, Crawley A (1993) Quantitative-evaluation of several partial fourier reconstruction algorithms used in MRI. Magn. Reson. Med. 30:51–59

[80] Weisman ID, Bennett LH, Maxwell LR, Woods MW, et al. (1972) Recognition of Cancer in vivo by Nuclear Magnetic Resonance. Science 178:1288–1290